3D PRINTED PHOTOACOUSTIC SHOCKWAVE TRANSDUCER FOR CAVITATION RESEARCH

CHAN WEIWEI

Interdisciplinary Graduate School
Nanyang Environment & Water Research Institute

A thesis submitted to the Nanyang Technological University in partial fulfillment of the requirement for the degree of

Doctor of Philosophy

2018

Acknowledgements

First of all, I would like to express my most sincere thanks to my main supervisor Prof Claus-Dieter Ohl for his visionary and patient guidance during the four years. I also wish to thank my co-supervisors, Prof Law Wing Keung Adrian and Prof Thomas Hies for their helpful advice in engineering and industrial aspects. I am thankful to all of my lab mates from Nanyang Technological University Cavitation Lab, and it is really my great honor to do research with them for the past several years. Then I wish to give my special thanks to Dr Chan Chon U, Dr Li Fenfang and Mr Zeng Qinyun for their encouragement and help during the study. At last, I would like to express my deepest gratitude to my dear parents, my maternal grandfather, Mr Jiang Menghua and Ms Xin Xin for their love, understanding, care and support all the way along.

Abstract

In this thesis we investigate a flexible ultrasound emitter whose working principle is based on photoacoustics and is manufactured with a 3D printer. The laser generated photoacoustic waves is focused thereby achieving several hundred bars of positive pressure in water. Previous designs employed concave glass substrates decorated with catalytically grown carbon nanotubes. Here, we show that arbitrarily shaped surfaces made of polymers and printed with 3D printers allow the generation of waveforms with complex temporal and spatial shape. For optimization of the acoustic performance several materials are tested. Detailed high-frequency pressure measurements are supported with shadowgraphy images and simulations of the wave. Applications of the new transducer are shown in sample experiments demonstrating shockwave–bubble interactions, interfacial cavitation and jets from a concave gas-water interface.

Table of contents

List of figures **ix**

List of tables **xiii**

1 Introduction **1**

2 Literature Review **5**

2.1 Laser induced high frequency ultrasound 5

2.1.1 Application of photoacoustic effect 13

2.2 Development of 3D printing 14

2.3 Introduction to bubble dynamics 16

2.3.1 Jet and meniscus 21

3 3D Compatible Photoacoustic Transducer **23**

3.1 Introduction 23

3.2 Characterization of the surface coating 24

3.3 Fabrication of LGFU transducers 27

3.4 Characterization of the transducers 30

4 Realization of arbitrary wavefront by the 3D printer and other fabrication approaches **39**

4.1 Introduction 39

4.2 Different designs of the transducers 40
4.3 Simulation of the pressure from structured transducers 42
4.4 Towards generating higher acoustic pressure 49
4.5 Alternative approaches to photoacoustic transducers 50
4.5.1 PDMS casting transducer 53
4.5.2 Droplet-based transducer 55

5 Interfacial cavitations induced by photoacoustic shockwave 59
5.1 Introduction 59
5.2 Experiment 60
5.3 Poly-dispersed bubble – shockwave interaction 61
5.4 Shockwave induced jet in the capillary tube 62
5.5 Cavitation and jet at the water-air interface 65
5.6 Cavitation at the water-glass interface 70
5.7 Cavitation and jet in the small droplet 73

6 Conclusion and outlook 77
6.1 Conclusion 77
6.2 Outlook and future work 79

Bibliography 81

List of figures

2.1 Illustration of photoacoustic effect on thermoelastic regime. 8

3.1 Sample preparation for testing blackout materials. 24

3.2 Experimental setup to test the planar transducer. The laser is collimated to a diameter of 1 cm, the laser energy is 8 mJ/pulse. 26

3.3 Pressure recordings emitted by the planar transducer with three different coatings are compared. 27

3.4 (a) 2D illustraion and (b) 3D sketch of the substrate for single wave excitation. The radius of curvature is 10 mm and the opening aperture is 15 mm in diameter. 28

3.5 Procedures to fabricate the light absorbing coating. 29

3.6 The photo of the real transducer. 29

3.7 Scanning Electron Microscope image of the light absorbing film. 30

3.8 Experimental setup to profile the spherical transducer. Reproduced from [1], with the permission of AIP Publishing. 32

3.9 Positive pressure amplitude versus laser fluence of the four susbtrate materials. Reproduced from [1], with the permission of AIP Publishing. 33

3.10 The pressure distribution along the central axis of the transducer of the spherical transducer of the four materials (at 10 mJ/cm^2). (a) shows the positive pressure, and (b) the negative pressure. Reproduced from [1], with the permission of AIP Publishing. 35

3.11 Methodology to scan pressure distribution in the horizontal focal plane. . . 36
3.12 Positive pressure distribution in the horizontal focal plane from the resin (a) and the glass (b) substrate. Reproduced from [1], with the permission of AIP Publishing. 36
3.13 (a) The pressure measurement at the focus; (b) the frequency spectra from the glass and the resin substrates, normalized to the maximum amplitude of the glass substrate. Reproduced from [1], with the permission of AIP Publishing. 37

4.1 Illustration of the the two stepped transducer: (a) 2D plot and (b) 3D model. 41
4.2 Pressure reading from the two-stepped transducer. 41
4.3 Illustration of the cross step transducer: (a) 2D plot and (b) 3D model. . . . 42
4.4 Pressure measurements of the cross transducer. 43
4.5 Simplified geometry of the two-stepped transuducer. 43
4.6 Comparison betweent the real experiment and the simulation (without fiber) 47
4.7 Reading from the probe near the focus without placing the fiber. 47
4.8 Reading from the probe near the focus with placing the fiber. 48
4.9 Comparison betweent the real experiment and the simulation (with fiber). . 48
4.10 Diffraction wave at the corner from calculation. 49
4.11 Illustration of the improved transducer to increase the pressure. (a) Spherical transducer; (b) two-stepped transducer. 51
4.12 Pressure reading from the improved spherical transducer. 51
4.13 Pressure reading from the improved two-stepped transducer. 52
4.14 Procedures to fabricate the transducer. 54
4.15 (a) PLA negative molds from Ultimaker and (b) PDMS casting transducer. . 54
4.16 Pressure measurements for the PDMS casting transducers of different mixture ratio (5:1 and 10:1, at the same laser exposure energy, $\sim$8 mJ/pulse). . . . 55

4.17 Procedures to make the droplet transducer. 57

4.18 The signal of the hydrophone from the droplet transducer. 57

4.19 Positive pressure measurements along the vertical direction away from the glass surface, where the errorbar indicates the standard deviation values from the scanning readings. 58

4.20 The pressure distribution contour in the focal plane. 58

5.1 Illustration of the experimental setup for poly-dispersed bubble – shockwave interaction. 61

5.2 Illustration of the experimental setup for poly-dispersed bubble – shockwave interaction 63

5.3 Small bubble cloud following the collapes of the laser induced bubble . . . 63

5.4 Expansion of bubble cloud, time interval of each frame 3 μs. (a) Case of the improved transducer with maximum pressure $\sim$500 bar; (b) case of the original setting transducer with maximum pressure $\sim$150 bar. 64

5.5 Bubble diameter versus time (with the improved transducer). The error bar indicates the standard deviation of the diameter measurements. 65

5.6 Illustration of the experiment of jetting in the glass capillary tube. 66

5.7 Jetting inside the glass capillary tube with time interval of 4 μs. 67

5.8 Height of the jet before it hit the inner wall of the tube, corresponding to Figure 5.7 68

5.9 Illustration of the experiment of the interfacial cavitation. 68

5.10 Cavitation at the water – air interface. The time interval between frames is 4 μs: (a) at full energy input 16 mJ/pulse; (b) at 8 mJ/pulse. 69

5.11 Cavitation size versus time at different settings of input laser energy 69

5.12 Jet at the water – air interface with time interval of 40 μs. (a) Splashed jet at the interface (with slow images with time interval of 5.5 μs); (b) Drop generated from the interface. 70
5.13 Illustration of the experiment of the water-glass interfacial cavitation. . . . 71
5.14 Hydrophone reading of cavitation on the water–glass interface 72
5.15 Cavitation on the water–glass interface, time interval of two frames 0.5 μs . 72
5.16 Illustration of the experiment for shockwave inside the droplet 73
5.17 The jet from the surface of a small drop with time interval of 10 μs 74
5.18 Jet height versus time, from the same experimental record of Figure 5.17, with time interval $\sim$3 μs. 74
5.19 Cavitation inside the droplet (white arrows show the cavitation inside the drop). Time interval 50 μs. 75

List of tables

2.1 Summary of the PA transducers in previous literature 13

3.1 Approaches to handle the photoacoustic surfaces 25

3.2 Material parameters related to the photoacoustic effect 31

6.1 Summary of the pressures of different types of transducers 78

Chapter 1

Introduction

This thesis concerns the investigation of the research on cavitation based on 3D printing photoacoustic transducer. Inspired by 3D printing technology, the basic idea is to fabricate the transducer by using different types of 3D printers, develop the flexible physical deposition method for fabrication of surface of the transducer and conduct cavitation-related experiments by using the novel device. The idea is then further developed to control the multiple wavefronts of different spatial resolution and amplitude by changing the geometry of the transducer. By taking the advantage of 3D printing, the device can be easily manipulated to various forms, including stepped transducer, axicon transducer and minimal size transducer in addition to the spherical shape. The ultimate expectation is to manipulate spatial, temporal and amplitude distribution of acoustic pressure so that the control of cavitation generation will be realized.

Previously, piezoelectricity is the most frequently used approach to generate ultrasound with high voltages. However, the performance is restricted in amplitudes and frequencies [2]. Previous efforts were made towards the direction to achieve acoustic wave with higher

pressure amplitude and frequency. In order to induce high amplitude and frequency (MHz to GHz level) focused ultrasound, photoacoustic effect was introduced. Photoacoustic pressure is based on the thermoelastic property of the coating materials on the transducer surface and excited by short laser pulses. Due to the short pulse width of the laser source (nanosecond level), the profile of the output acoustic pressure can reach very high frequency to even GHz level. Meanwhile, it can be a durable and non-destructive process, which does not require high voltage input. Previous research has already shown some fabrication methods with glass [3, 4]. The photoacoustic effect can induce a series of phenomena with interfaces and bubbles, which is the main interest in this thesis.

In this thesis, we demonstrate three 3D-printing techniques for laser induced focused ultrasound (LGFU) transducers, and one of them reveals similar if not a better performance than a glass substrate. Different types of 3D printers, including stereolithography (SLA), selective laser sintering (SLS) [5], fused filament fabrication (FFF), were utilized. In particular, we discuss the fabrication of the transducer substrate and coating with a Polydimethylsiloxane-Carbon nanotube (PDMS-CNT) mixture paint. Then we measured the acoustic waves temporally and spatially resolved before we presented a complex waveform generated from a stepped surface using shadowgraphy imaging and compare the results with simulations. We also managed to fabricate the transducers of other geometries. After improvement, the positive pressure of the transducer could be increased to 500 bar with spatial resolution smaller than 500 μm. We also introduce some auxiliary fast approaches to fabricate minimal scale transducers to generate focused photoacoustic pressure on the flat solid surface with high spatial precision. We also explored how the photoacoustic waves behaved with differ-

ent interfaces, bubbles, and the capillary tube. The photoacoustic pressure induced strong phenomena of cavitation and jets at the interface. It could also enhance bubble oscillation when meeting with the laser induced bubble cloud. However, we failed to generate bubbles in free field of liquid, which we expected to be useful in further applications. Future work will be focused on free field cavitation, small integrated devices and sophisticated design of transducers.

Chapter 2

Literature Review

2.1 Laser induced high frequency ultrasound

Ultrasound refers to the acoustic waves with the frequency higher than maximum human hearing limit of 20 kHz [6]. The range can be varied from 20 khz to giga hertz level. Ultrasound has been found, developed and utilized in many research and application fields through the past hundred years, such as real-time imaging, cleaning, drug delivery and biomedical therapy due to its non-invasive and accurate performance [2, 7–10]. There are different mechanisms to generate ultrasound, including piezoelectricity, and photoacoustics [7]. Piezoelectricity is the most common approach to produce high frequency ultrasound below 10 MHz [11]. The piezoelectric transducer responds to the AC voltage. The shape of the transducer changes with the voltage periodically. This process usually requires high voltage input. A potential alternative method to generate high frequency ultrasound in liquid is to follow the photoacoustic principle [12, 13]. The photoacoustic effect was first observed in 1880 [14]. The sound was emitted from a plate when the white light was shone on the

plate. The white light source was controlled by a shutter. Nowadays, in order to obtain high frequency and energy intensive acoustic signals, laser is utilized to trigger the effect due to its high energy intensity and narrow bandwidth of 20 ns [3, 15]. In addition, the light absorbing materials do vary [3, 4, 16]. Metals, such as aluminum, gold and chromium, can be applied as the light absorbing materials. Recently, researchers found the potential of carbon based materials competitive in absorbing light an converting into heat.

There are different mechanisms for generating photoacoustic waves, including dielectric breakdown, vaporization [13], and thermoelastic process [13]. According to the literature [17], the extremely high laser power was applied on the materials and caused the material to be breakdown and emit one-time acoustic pressure. The energy conversion efficiency of dielectric break is the highest among all the mechanisms, which is up to 30 % [17]. Vaporization can also lead to photoacoustic effect. When the light-absorbing surface absorbs the energy, which exceeds the boiling threshold of water, vapor will be generated near the surface and pressure will be induced. The efficiency can be 1 % [17]. The most interested mechanism in this thesis photoacoustic effect is thermal expansion of the material, i.e the thermoelastic effect [13]. The thermoelastic effect is induced by localized transient heating of a certain volume of material. A plate with a light absorbing film on it is exposed under a pulsed laser. The light-absorbing material absorbs light and transforms optical energy into heat. The thermoelastic material absorbs heat and experiences localized thermal expansion. The heat conduction inside the thermoelastic material is nearly negligible during the laser excitation time ($\sim$6 ns). Thermal confinement of the material occurs due to the short pulse

width of the laser, which can be described by Eq.2.1 [18],

$$\nabla^2 p(\vec{r},t) - \frac{1}{v_s^2}\frac{\partial^2}{\partial t^2} p(\vec{r},t) = -\frac{\beta}{c_p}\frac{\partial}{\partial t} H(\vec{r},t) \tag{2.1}$$

Figure 2.1 depicts the arrangement to create photoacoustic waves; the laser is illuminating an absorbing layer through a transparent substrate. The light absorbing layer contacts with water and emits photoacoustic wave into the liquid.

The frequency spectrum of photoacoustic wave is dependent on the pulse width of the input laser pulse [18]. Two conditions, thermal and string confinement, should be met to generate photoacoustic wave efficiently [33]. Heat diffusion is dependent on the geometry of the heated volume. Therefore, the thermal conduction time is varied. The pulse width of the incident laser should be shorter than the thermal conduction time in order to make the process efficient. Similarly, the transition of the string should also meet such a condition, where the pulse width of the laser should be smaller than the string transit time in the material. Thus, it is possible to achieve high frequency signals up to MHz and even GHz level compared to piezoelectric technologies, if the nanosecond width light source is utilized appropriately [11]. The temporal profile of a excited PA signal is locally related to the light absorption and scattering structure of the light absorbing film [33]. The thermoelastic regime of photoacoustic effect is attractive due to the non-destructive and reversible features to the material. However, thermoelastic expansion suffers from lower conversion efficiency of 1.3×10^{-6} traditionally than piezoelectricity method [11, 13].

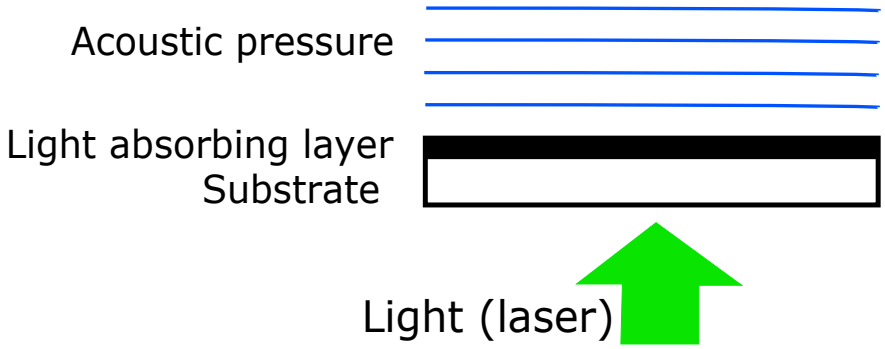

Fig. 2.1 Illustration of photoacoustic effect on thermoelastic regime.

Previous research has developed a mathematical model for the photoacoustic wave based on the temperature variation in the light absorbing material [19]. It can be expressed by the thermal-mechanical coupled form of the wave equation, as in Eq. 2.2 and 2.1, where P_i is the induced pressure, C_{Li} is the sound velocity in liquid, C_{Pi} is the specific heat capacity of liquid and $\hbar_i$ is the heating function. Here, the light absorbing film is considered as elastic. The damping and viscous effects of the liquid are not taken into account.

$$\nabla^2 P_i - \frac{1}{C_{Li}^2}\frac{\partial^2 P_i}{\partial t^2} = -\frac{\beta_{Ti}}{C_{Pi}}\frac{\partial \hbar_i}{\partial t} \tag{2.2}$$

Effort has been made towards achieving higher precision (smaller spatial resolution), higher acoustic pressure and frequency [3, 20, 21]. To excite a strong photoacoustic pressure, three factors are dominant in designing a photoacoustic device, i.e. optical absorption, thermal transduction and thermal expansion [3]. Currently, polymer is the promising choice for the high thermal expansion. Specifically, the polydimethylsiloxane (PDMS) is considered as one optimum option [22, 23]. Interestingly, PDMS has stable thermal properties except for its significant volume thermal expansion of 0.2×10^{-5} K^{-1} [3]. As for the light-absorbing

film, carbon-based material is considered as a promising option [16, 21, 23]. Previously, carbon black has been used as the light-absorbing material to enhance the pressure amplitude by 24 dB comparing with the reference chromium film [11]. Recently, along with the development of carbon nanofabrication, carbon nanotubes and carbon nanofibers are utilized as an efficient light absorber [7, 16]. Most of the carbon-based materials can be deemed as candidates in inducing photoacoustic effect. Even the candle soot can be considered as a convenient alternative to fabricate light absorbing surface [4]. Here, we focus on carbon nanotubes. Carbon nanotubes (CNTs) have efficient capacity in transforming light into heat. This property of CNT shows promising improvements for the photoacoustic effect with significantly increased conversion from optical energy to acoustic pressure. Theoretically, for a given dimension of the carbon nanostructure, after being exposed to laser light, the fraction of generated heat, with respect to pulse duration of the later, η, is estimated by Eq. 2.3 [24],

$$\eta = \frac{\tau_{HD}}{\tau_L} \times [1 - exp(\frac{\tau_L}{\tau_{HD}})] \tag{2.3}$$

where τ_{HD} is the heat diffusion time and τ_L is the laser pulse duration. This equation concludes that most of the generated heat is transferred to pressure and the time for the CNT to diffuse heat to surrounding PDMS is negligibly short [23]. The high frequency signal is largely influenced by the thickness of the absorber material. The acoustical attenuation increases as the thickness of the material increases [15]. In order to precisely control the thickness of the absorption layer, chemical vapor deposition (CVD) can be used to grow the carbon nanotube layers on the substrate [3, 15].

Metal was also considered as a candidate of light absorbing surface. Surface plasma refers to the electron oscillation which exists on the interface of two materials (like air and metal). The oscillation of these electrons will induce electromagnetic field nearby [25]. Especially for most nanostructure, the localized surface plasma is significant [26]. The electromagnetic field is stronger and the material will have strong light absorption at resonance frequency of the electrons. The optical absorption of gold nanoparticles (AuNPs) technology is strongly dependent on the size and shape due to the surface plasma. AuNP is able to absorb light of wavelength ranging from 550 nm to 600 nm efficiently [2]. AuNPs can be used in two ways. Due to its absorption property, it can be utilized as an optical absorber. Otherwise, it is possible to apply it as a reflector, thus increase optical extinction of the surface. It is well studied that the two-dimensional gold nanostructure is applicable to generate high frequency ultrasound [27, 28]. AuNP films are coated on the PDMS layer by nanoimprint lithography technique [27, 29]. The frequency of acoustic pressure can reach over 50 MHz. Such a high frequency is severely relevant to fast heat transfer rate. With the input optical power of 100 nJ and beam spot size of 25 μm, the photoacoustic pressure near the surface represents 1.5 MPa [27]. Besides AuNPs, other gold nanostructure is also possible being produced by mixing the gold salt powder and PDMS matrix to induce photoacoustic pressure [27]. Table 2.1 shows a summary of previously achieved photoacoustic pressure of different types of photoacoustic transducers.

Besides the importance of the light absorbing material, the gain through the spherical converging wave is important. The gain factor of the photoacoustic transducer summarizes the gain in pressure from the surface of the transducer to the focus. Its functional dependency

with the acoustic frequency f, the sound speed in the liquid c_0, radius of curvature of the transducer r and the f-number f_N (which is the ratio between the radius of curvature to the lens diameter) is [30]:

$$G = \frac{2\pi f}{c_0} r(1 - \sqrt{1 - \frac{1}{4f_N^2}}) \tag{2.4}$$

Eq. 2.4 demonstrates the importance of a large curvature for high gain. Shockwaves have been observed near the focus point and the acoustic signal reached to over 100 bar [3]. Theoretically, photoacoustic pressure waveforms are similar to Gaussian form [30]. For a pulsed laser source, the photoacoustic waveform is found to be proportional to the temporal profile of the laser pulse in one dimension, the (l/2)'th time derivative of the laser pulse in two dimensions and the first time derivative of the laser pulse in three dimensions [31]. The relation between the pressure and time-derivative profile of the input laser can be described by [3, 19],

$$p = \frac{1}{4\pi} \frac{3B^2\alpha_L}{\rho c^2} \frac{1}{r} \frac{\partial I}{\partial t} \tag{2.5}$$

where B is the bulk modulus, α_L is the linear thermal expansion coefficient, ρ is the water density, r is the distance away from the thermoelastic source, and $\frac{\partial I}{\partial t}$ is the time-derivative profile of the input laser. The principle of generating shock waves can be explained by nonlinear propagation of the acoustic pressure pulse in positive and negative phases [3]. The

photoacoustic generation efficiency is another important parameter in research. As studied before, the energy converting efficiency is the equation defined by Eq. 2.6 [32],

$$\eta = \frac{E_a}{E_{optical}} \tag{2.6}$$

which is the ratio between the generated acoustic energy E_a and the input optical energy $E_{optical}$. The acoustic pulse energy is dependent on the sound velocity in water c, bulk modulus of water B, acoustic press p and laser beam area A, by Eq. 2.7 [3],

$$E_a \cong \frac{c}{B} A \int_0^\infty p^2(t) dt \tag{2.7}$$

Currently, the direction of photoacoustic research is towards boosting generation efficiency and achieving higher frequency. We can apply the photoacoustic effect in controlling the waveforms with the help of 3D printed transducers. It seems that the photoacoustic principle has the potential to be adapted and used for manipulating waveforms. For the preliminary trials of the experiment, we utilized the black nailpolish as the absorbing materials due to its polymer components and black color, which are satisfactory in thermal expansion and optical absorption. The nailpolish is easy to approach and coat on the surface. As trials, it is more feasible than powders. In later chapters, we tried to apply different carbon-based materials, including CNT powder, reduced graphene oxide and candle soot.

Table 2.1 Summary of the PA transducers in previous literature

Type	Max positive pressure (bar)	Shape
Glass-based [3] and CNT	220	Spherical
Candle-soot [4]	45	Planar
Au Nanoparticles [27]	15	Planar
Carbon nanofiber [16]	120	Planar
Reduced graphene oxide [34]	7.5	Planar

2.1.1 Application of photoacoustic effect

Photoacoustic effect has already been applied in biomedical imaging [33, 35]. It can further boost the performance of ultrasonic imaging due to its high frequency and broad bandwidth. The so-called photoacoustic tomography can clearly take images of the mouse brain tissue [36] with the help of optical agents. It shows advantages of resolution, contrast and speckles in contrast with traditional pure optical and pure ultrasonic imaging method, like photodiode imaging and B-mode ultrasonography [37]. This method has also been proven effective in penetrating thick body tissue for medical diagnosis [38].

Recent reports showed potential of the photoacoustic effect for medical therapy, in particular for tissue removal and needle-free injection. The high frequencies of the photoacoustic waves allow for micro-scale penetration of soft tissues, like agarose gel and localized indentation on hard materials, like aluminum foil [3, 39, 40]. The glass photoacoustic transducer

has been demonstrated the capability to induced cavitation and microbubbles at different interfaces and free-field water [20]. Previous literature also mentioned the jet induce by photoacoustic pressure, which may be used for high resolution inkjet printing [40].

2.2 Development of 3D printing

The term "3D printing" describes the manufacturing process of an object by adding material. This additive manufacturing (AM) process is distinct from conventional manufacturing which uses the removal processes to shape the object, e.g. with a mill or a lathe; yet the design process shares similarities: it starts with an object's geometric representation in 3 dimensions (3D) and the slicing of the object into layers to calculate the tool paths. In 3D printing, the tool paths are for building up the objects whereas in subtractive manufacturing the tool removes the material.

3D printing has irreplaceable advantages compared with conventional manufacturing process [41, 42]. 3D printer performs flexibly in manufacturing physical objects of complexity [42], even those which are not friendly to machinery. Thus, it is also friendly to designers for developing the objects with more organic, complex and customized structures. The selection of materials for 3D printing is various to fulfill different functions of the objects, ranging from metal, glass, plastics, ceramics to even bio-tissues [41, 43, 44]. The potential applications of 3D printed objects land in many usages, from simple plastic models to even human organs for implantation and devices in automobile and aerospace industry [41, 43, 44]. Moreover, it saves a considerable large amount in material, time and cost consumption due to its precise

prototyping [42]. However, researchers are still making effort in implementing standard and reliability of 3D printed objects for real industrial use and public markets [41].

3D printing has experienced explosive development since the rise of the initial idea in early 1980s [45]. There are several well established prototype models of 3D printers, mainly including stereolithography (SLA), selective laser sintering (SLS) [5], fused filament fabrication (FFF) or fused deposition modeling (FDM), laminated object manufacturing (LOM) and and inkjet printing techniques [43]. Other minor methods like prometal, electron beam melting and 3DP are also innovated [41]. They exhibit different qualities and strengths in real manufacturing processes. As in FFF (or FDM), the printer melts the thermoplastic material, such as acrylonitrile butadiene styrene (ABS) and polylactic acid (PLA), into liquid stripes and extrude stripes from the nozzle. The liquid stripes will be solidified quickly after leaving the hot nozzle. The liquid from the hot nozzle will fabricate the object according to the computer-generated machine code line by line, and thereafter layer by layer. This type of printer has already been widely used in both research and home-making design due to the economical materials and lower price of the machine. The materials for 3D printing are varied depending on different situations. The 3D printing materials are various through development, including thermoplastics, glass, bio-tissues, ceramics and metals. It is also possible to print multiple material objects.

SLA and SLS both require laser in manufacturing process. SLA applies the UV laser light to cure the liquid printing materials, like resin [46]. The laser causes the link of liquid polymer and solidifies the liquid to targeted model. This method can print the object from top or bottom, thus, it is friendly in printing items of wide size range from hundreds of

micrometer to meter scale [47]. This approach has the highest accuracy among all the current printing mechanisms [41], meanwhile it is the second most costly method. SLS is also an accurate printing method. The mechanism is to sinter and then binding materials by focusing the high power laser at the targeted points on the bulky material as controlled by the code. It can be used for various materials like glass, ceramics and metal alloys, which usually require high temperature to melt. SLS can print the object with good strength. However, the cost is higher and the process requires more energy and time. SLS can be used to produce large size items [43].

There are other printing methods, such as laminated object manufacturing (LOM) and inkjet printing technique. They stand out for lower cost and less energy consumption, but meanwhile limited to quality and strength. LOM is the method in which plastic or paper layers are cut by the laser cutter and adhered together as an object. Inkjet printing is to use the piston for dispensing fine powders and adhere the layer of powder to another by the liquid ejected by another piston [41, 48].

2.3 Introduction to bubble dynamics

Cavitation arises from the strong rupture of liquid and bubbles induced from cavitation are named cavitation bubbles [49]. The schemes of cavitation generation can be attributed into two main campaigns [49], tension and energy deposition. Tension, i.e. negative pressure, ruptures liquid and forms cavitation. Acoustic devices, like transducer can be used to generate cavition in this way [50]. The time-dependent acoustic pressure stretches liquid and generates

cavitations. Energy deposition can be done by particles, heat and light to form cavitation in the liquid. A variety of devices can be utilized for bubble generation by the mean of energy deposition. For example, one convenient approach to produce one single bubble is to focus a laser beam to a small spot in liquid [51]. The size, oscillation and lifetime of the bubble can be controlled through varying the performance parameters of the input laser [52, 53], like the energy of laser and location in the container.

The simplest case of bubble is the single stable bubble. A single stable bubble in the liquid acts like an oscillator which vibrates between the maximum and minimum radii under an external time-dependent pressure field. There are several important parameters used to model the oscillation of the bubble in liquid. For the simplest case, the bubble radius R is related to time t, the bubble radius at rest R_n, the liquid density ρ and the external pressure field p_e. This simplest model to describe a single bubble has been developed by Rayleigh and expressed as the Rayleigh bubble model [54],

$$\rho R\ddot{R} + \frac{3}{2}\rho\dot{R}^2 = -p_e \tag{2.8}$$

Eq.2.8 describes the situation where the void bubble is placed in an infinitely large liquid volume. If a bubble expands to the large maximum radius, it will undergo a rapid shrinkage which is not anymore governed by the driving acoustic frequency. This response is called cavitation bubble collapse. During collapse, high temperature, very fast velocity, and acoustic emissions will occur [55]. The Rayleigh collapse time, i.e., the time for a bubble to collapse,

is thus derived as Eq.2.9,

$$t_{Rayl} = 0.914 R_0 \sqrt{\frac{\rho}{p_0}} \tag{2.9}$$

where R_0 is the initial radius of the bubble and p_0 is the constant pressure for reference [56]. This model neglects many important physics parameters, for example, the effect of surface tension, temperature and liquid viscosity. Yet it gives a good approximation for the gross dynamics and time of shrinkage of the void bubble [55]. An improved model which accounts for viscosity of liquid, surface tension and bubble content is developed, known as the Rayleigh-Plesset model. This model is used for the case of vapor and gas bubbles with the assumption that the bubble interior is homogeneous with uniform temperature and pressure. We can use this model to describe an single oscillating bubble. The driving pressure is introduced through a time varying pressure located far from the bubble. The Rayleigh-Plesset model is described as Eq.2.10 [55],

$$\rho R\ddot{R} + \frac{3}{2}\rho\dot{R}^2 = p_{gn}(\frac{R_n}{R})^{3\kappa} + p_v - p_{stat} - \frac{2\sigma}{R} - \frac{4\mu}{R}\dot{R} - p(t) \tag{2.10}$$

where $p_{gn} = -p_v + p_{stat} + \frac{2\sigma}{R}$, is the gas pressure inside the bubble at the steady state, σ is the surface tensor, *p(t)* is the driving pressure, commonly assumed of a sinusoidal form as in Eq.2.11),

$$p(t) = -p_a sin(2\pi v_a t) \tag{2.11}$$

and μ is the dynamic viscosity of the liquid. The Rayleigh-Plesset model is derived based on mass conservation, momentum conservation and the boundary condition that the pressure at r=R equals to the summation of the surface tension, normal viscous stresses and the

pressure inside the bubble. This model has been developed further to account for liquid compressibility and heat and mass exchange. For example, the Keller-Miksis model as Eq. 2.12 [57] and the Gilmore model as in Eq. 2.13 [58] incorporate the compressibility of the liquid and thermal effects. Details and references to the vast literature available are discussed in the review paper by Lauterborn and Kurz [54].

$$(1-\frac{\dot{R}}{C})R\ddot{R}+\frac{3}{2}(1-\frac{\dot{R}}{3C})\dot{R}^2=(1+\frac{\dot{R}}{C})\frac{p_1}{\rho}+\frac{R}{\rho c}\frac{dp_1}{dt} \tag{2.12}$$

$$(1-\frac{\dot{R}}{C})R\ddot{R}+\frac{3}{2}(1-\frac{\dot{R}}{3C})\dot{R}^2=(1+\frac{\dot{R}}{C})H+\frac{\dot{R}}{C}(1-\frac{\dot{R}}{C})R\frac{dH}{dR} \tag{2.13}$$

where C is the speed of sound in liquid and H is the enthalpy.

The bubble oscillation can be described with an amplitude response (resonance) curve like other kinds of oscillators [54]. Although the Rayleigh-Plesset model is a non-linear oscillator [54], it shows, for an sufficiently low driving pressure amplitude, a single resonance similar to a harmonic oscillator. Minnaert [54] has obtained an analytical expression for this linear resonance in absence of viscous damping. He modeled the gas with a polytropic exponent κ. The resonance frequency of a single bubble is derived as:

$$v_0=\frac{1}{2\pi R_n}\sqrt{\frac{3\kappa p_{stat}}{\rho}} \tag{2.14}$$

In water, Eq.2.14 can be simplified further to [54],

$$v_0 R_{n0}\approx 3ms^{-1} \tag{2.15}$$

where v_0 is the resonance frequency of Rayleigh-Plesset model. However, in real situations, bubbles will not keep a spherical geometry all the time [55]. During the rebound phase, its geometry may become unstable and the bubble splits into daughter bubbles. These may or may not coalesce during the bubble rebound. For a strong external driving to the system, the bubble becomes nonlinear and additional resonance will appear at higher or lower frequencies than the excitation frequency, i.e. the superharmonics ($n\omega$, ω is the driving frequency and n is the positive integer) and the subharmonics ($m\omega/n$, m and n are positive integers) [55].

Shockwave is a phenomenon of strong flow disturbance in fluid. It happens when the acoustic wave travels faster than the local speed of sound in fluid [59]. The ratio of the traveling speed of the acoustic wave to the local sound speed is so-called Mach number [60]. Shockwave always carries large amount of energy and leads to sudden changes in temperature, pressure and density of the fluid. The explosive bubble formation always accompanies with shockwave [40, 56]. Bubbles react differently when a shockwave passes by [61]. The bubble will experience sudden and strong compression in the short process. The properties of the bubble change largely due to the passage of the shockwave. Non-linear acoustic effect will arise due to the shockwave. The shockwave itself is refracted, reflected and diffracted upon the presence of the bubble during propagation. The boundary of bubble plays as an interface inside water. The content inside the bubble and liquid outside the bubble lead to the acoustic impedance mismatch.

2.3.1 Jet and meniscus

Meniscus is the curved surface at the top of the liquid due to the surface tension. It is an exhibition of capillary action. The height of the meniscus h can be defined by Jurin's law as Eq. 2.16 [62],

$$h = \frac{2\gamma cos\theta}{\rho g r} \tag{2.16}$$

where γ is the surface tension of the water-air interface, θ is the contact angle, r is the radius of the capillary tube, ρ is density of liquid and g is the gravitational acceleration. The shape of the meniscus can be either concave or convex depending on hydrophobicity or hydrophilicity of the inner side of the container [63–65]. In the usual room condition, the height of the meniscus is calculated by,

$$h \approx \frac{1.48 \times 10^{-5}}{r} m \tag{2.17}$$

The common mechanisms of generating jets at the liquid surface include bubble bursting [49], impulsive acceleration of liquid surface and high amplitude Faraday waves [66–68]. All the cases result in kinematic focusing in the liquid. When the liquid surface becomes concave impulsively, the jet will be generated.Previous research has developed a lot in producing jet at the free liquid surface [69–71]. Jet induced by the laser has been well-developed for a long time [71, 72]. Through this method, the jet in a droplet could reach 250 m/s but failed to control the properties of the jet [72]. Jet can also be produced in a restricted liquid, such as in the microtube (capillary tube). Researchers utilized the microtube in the experiment. The limited space of the hollow structure of the microtube leads to the extremely fast acceleration

of the liquid surface when the laser spot is applied inside liquid. This approach could control the location, size of the jet as well as reduce energy input. The fastest velocity of the jet in this case could be up to 850 m/s with the jet size of 50 μm [63–65].

Previous literature [63] has revealed that the jet in the capillary tube is relevant to the contact angle of the Meniscus in the tube θ, absorbed energy by liquid E, the diameter of the capillary tube D and focus offsets. The equation is derived as Eq.2.18 to describe the jet behavior,

$$V_j \simeq C_0 \frac{(E - E_{heat})(1 + \beta cos\theta)}{HD} \tag{2.18}$$

where E_{heat} is the energy threshold below which the jet will not be produced, H is the increasing distance of the jet and β is the fitting constant. The velocity of jet was proved to be inverse proportional to the diameter and the distance of the laser spot away from the liquid surface.

The highly focused supersonic microjet from the capillary tube has a promising blueprint in medical applications, plasma spraying and cleaning [40, 73]. Recent research results have shown that the high speed jet could penetrate into gelatin through artificial human skin with high precision at the location with limited scattering [65]. The high speed jet can also be considered to be applied in high resolution inkjet printing [64].

Chapter 3

3D Compatible Photoacoustic Transducer

3.1 Introduction

We tried to find a suitable light absorbing coating which possesses a high light absorption coefficient and excellent heat diffusivity under exposure to a pulsed green laser light at wavelength of 532 nm . Previous researchreference has revealed that carbon based materials are good candidates for photoacoustic wave generation while absorbing at $\lambda = 532\,\text{nm}$. We experimented with four different coatings compatible with the polymer surfaces: black nailpolish (O.P.I, North Hollywood, CA, USA), carbon nanotube powder (ceEnTek, Pte. Ltd, Singapore), graphene oxide (Sigma Chemical) and candle soot. Besides the material, we need to device a suitable method to coat the light absorbing layer on a transparent substrate, in particular for low melting point polymer surfaces the gold standard of chemical vapor deposition is ruled out. Besides the coating and deposition, also the substrate material has an

effect on the photoacoustic wave generation efficiency. We used three different 3D printer material combinations for the fabrication of the transducer substrates and compare their performance.

3.2 Characterization of the surface coating

The transducer operates under water and is exposed to high laser power intensity (output of the laser of maximum value of 8 mJ/pulse). The high bandwidth and results in short wavelengths. Thus the surface needs to smoothen on the scale of the wavelength, e.g. at the wavelength is 150 μm at 10 MHz. The water should not sip in between the substrate and the coating, and the coating should be thin as it may absorb the acoustic wave at high frequencies. To test the different coatings, we made planar transducers composed of thin glass plates (50 $\times$ 70 $\times$ 1 mm). We chose four blackout materials as candidates, including multiwall carbon nanotube powder, nailpolish, graphene oxide water solution and candle soot particles. The approaches to coat the four materials onto the glass surface were different due to different conditions of the materials.

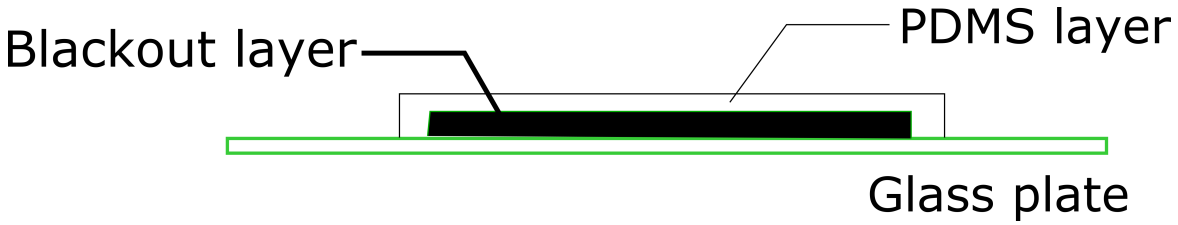

Fig. 3.1 Sample preparation for testing blackout materials.

The glass plates were first cleaned with acetone and ethanol successively in an ultrasonic water bath (Sonorex Digitec, Bandelin), and blown dry with nitrogen gas. Later processing

approaches were physical deposition, including brushing, smudging and evaporating, as listed in Table 3.1. There was no chemical or high temperature process (>100°C) involved. The coating area was a square of 1.5 cm $\times$ 1.5 cm. The specific steps for each material are listed in Table 3.1. After the light absorbing materials were firmly attached on the glass plates, a thin layer of PDMS (Sylgard 184, polymer to current agent ratio 10:1) was deposited on it by the spin coating machine (Spincoating, Germany, SPIN150-NPP, 2000 rps, 1 minute). The planar transducers were then place in an 80°C hot oven (Thermo Scientific Heratherm Advanced Protocol Oven, 61L) for curing the PDMS for 30 minutes.

Table 3.1 Approaches to handle the photoacoustic surfaces

Material	Approach	Result
CNT	Mixed with PDMS,Brushed, and covered with PDMS.	Firmly attached
Nailpolish	Brushed	Firmly attached
Graphene oxide	Evaporated, and covered with PDMS	Peeled off from glass and failed to attach
Candle soot	Smudged and covered with PDMS	Firmly attached

Not all materials could firmly stay on the surface of glass. We noticed that during the fabrication process, graphene oxide water solution was not suitable for coating on the glass surface. After evaporating, the layer of dried GO film cracked and peeled off the glass surface. The other three materials can firmly attach on the hard surface of glass to form a light absorbing layer, which are also durable after immersing in water for a long time (over months without great change in performance). Carbon nanotube powder, nailpolish and candle soot where then used the experiments to characterize the performance for generating photoacoustic waves.

The planar transducer was placed at the bottom of the tank which was filled with deionized water and exposed to a 532 nm laser pulse of 6 mJ. The illuminated range is a circular area of diameter of $\sim$ 1 cm. A hydrophone (Onda, HNR-1000, Sunnyvale, CA, USA) was placed at a distance of approximately 2.0 mm to record the emitted pressure. Figure 3.3 summarizes the results for the three coatings at constant laser energy and illuminated area. The highest pressure is emitted from the CNT coating reaching about 9.0 bar, candle soot and black nailpolish result into lower a peak pressure of about $4-5$ bar.

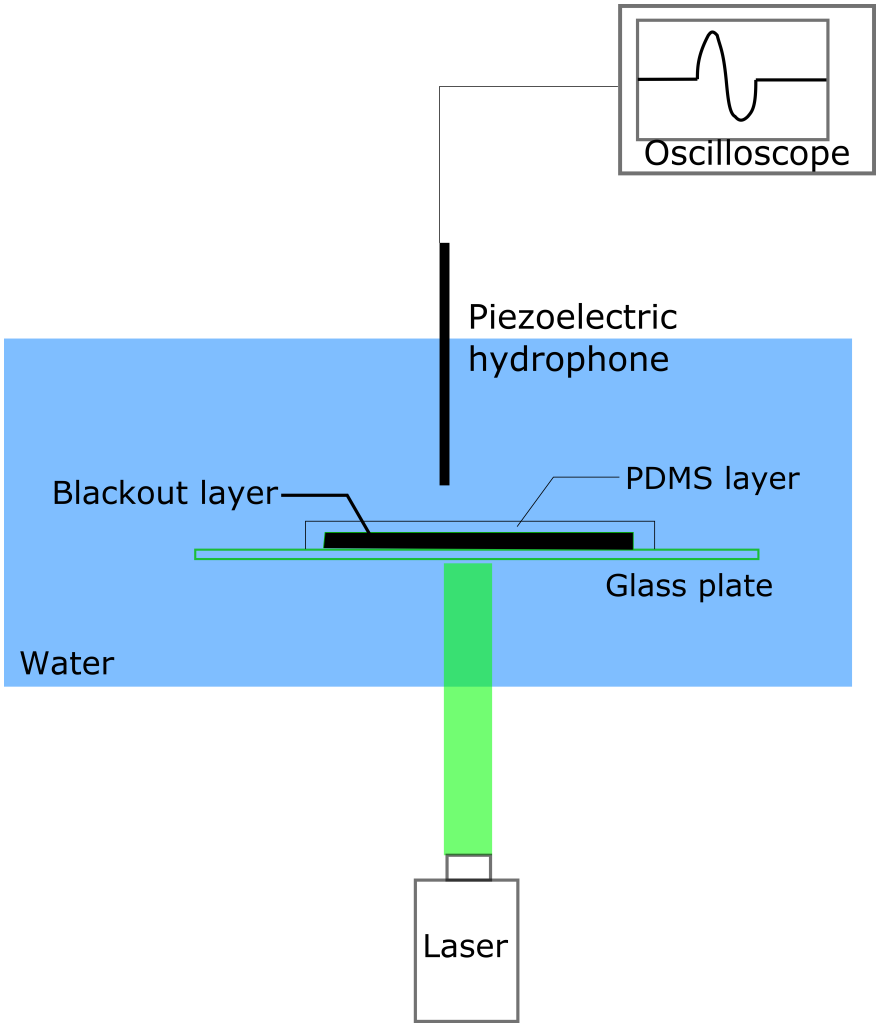

Fig. 3.2 Experimental setup to test the planar transducer. The laser is collimated to a diameter of 1 cm, the laser energy is 8 mJ/pulse.

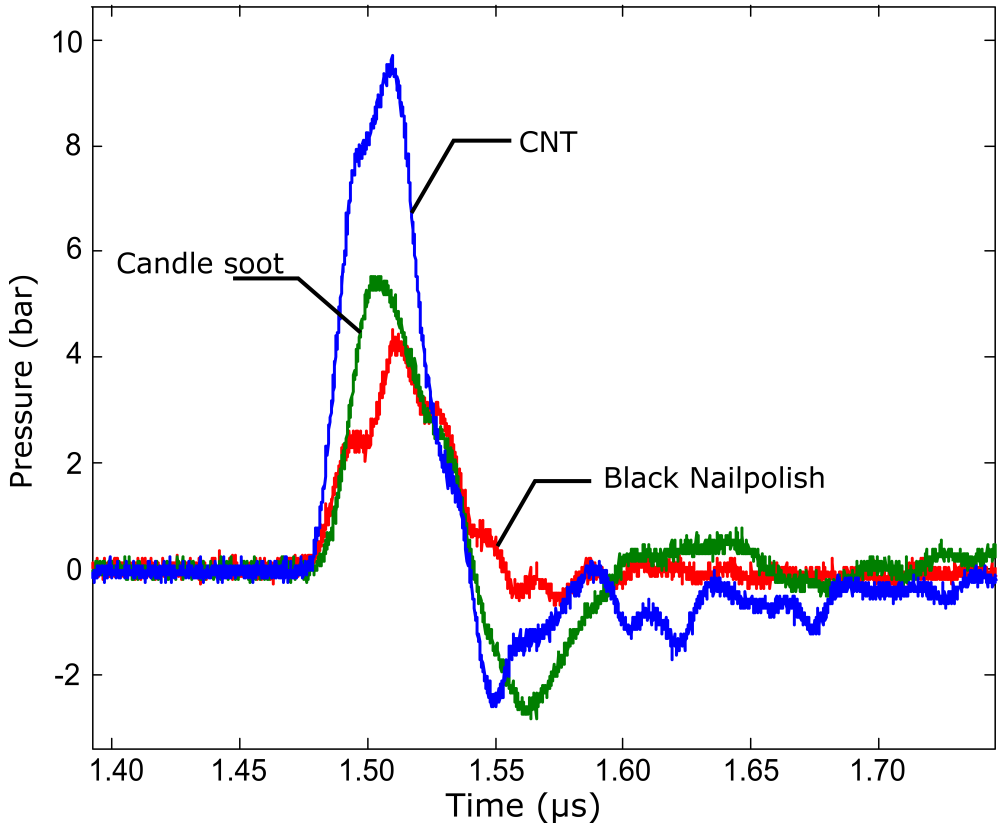

Fig. 3.3 Pressure recordings emitted by the planar transducer with three different coatings are compared.

3.3 Fabrication of LGFU transducers

Besides the light absorbing material, the material of the substrate plays a role in determining the performance of the transducer. The substrates not only supports the light absorbing materials, it also receives part of the acoustic wave generated in the coating. Next we evaluate three different materials combined and also try out three techniques to fabricate the LGFU transducers. For characterization of the spatial and temporal profiles are measured.

We chose for the following 3D printers to shape the substrate: a filament-based printer (Ultimaker 2, Geldermalsen, the Netherlands), a high-resolution jet printer (Objet Eden260VS,

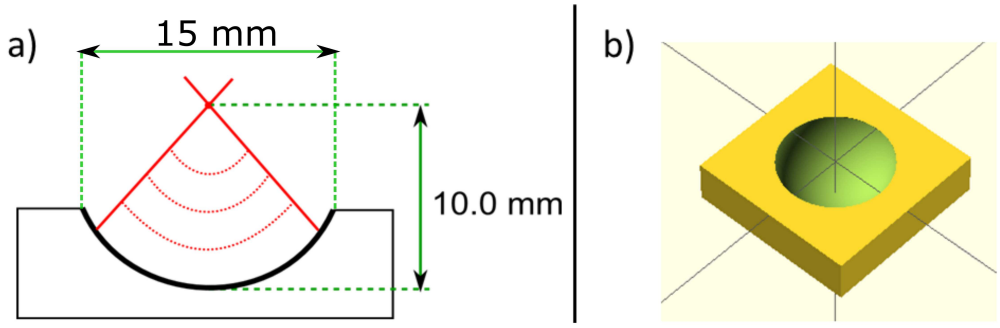

Fig. 3.4 (a) 2D illustraion and (b) 3D sketch of the substrate for single wave excitation. The radius of curvature is 10 mm and the opening aperture is 15 mm in diameter.

Stratasys, Eden Prairie, MN, USA) and a stereolithography printer (Formlabs+, Somerville, MA, USA). The materials of the mold are polylactide(PLA), VeroClear (RGD 810, Stratasys, Eden Prairie, MN, USA) and clear resin (Clear, FLGPLC02, Formlabs,Somerville, MA, USA). The molds printed by the stereolithography printer and the high-resolution jet printer can be directly used as substrates. In contrast, for the filament printer a negative mold was printed. The surface was then smoothened by exposure of the substrate to acetone and then the substrate was casted with transparent PDMS (Sylgard 184, polymer to current agent ratio 10:1). The full fabrication method is in Chapter 4. As a reference substrate material we use a BK7 glass negative lens (Thorlabs, N-BK7 Series) with radius of curvature of 15.4 mm to match the printed substrate shapes.

The method to coat the substrate with the light absorbing film on the 3D printed substrates is shown schematically in Figure 3.4. The first layer of carbon nanotube powder was deposited directly on the surface of the substrate. The second layer of PDMS was first dropped on the transducer and then spun with the spin coating machine to cover the first layer. The coating was cured at 80 °C oven for 30 minutes. These two steps were repeated once more to add two

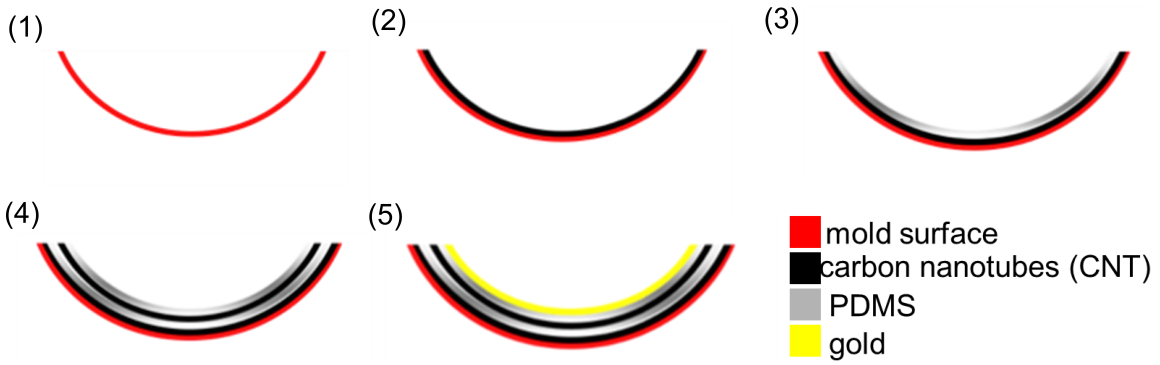

Fig. 3.5 Procedures to fabricate the light absorbing coating.

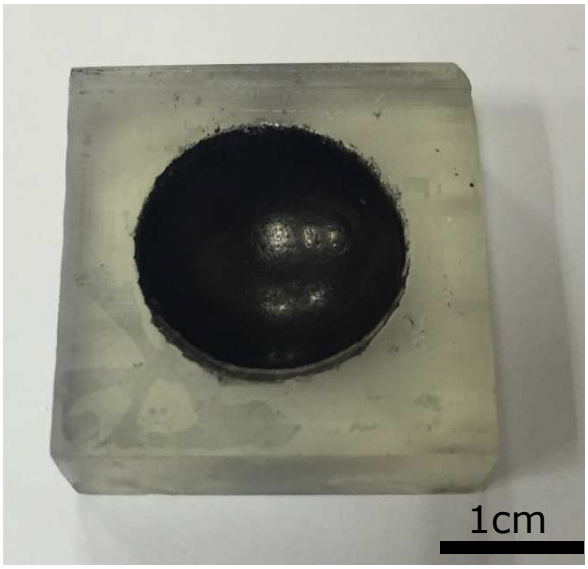

Fig. 3.6 The photo of the real transducer.

more layers. Lastly, a layer of golden nanoparticles was deposited with a sputtering machine (JEOL, Ltd, Akishima, Tokyo, Japan) at 10 mA current for 60 s. Through this method the thickness of the film is controlled to be thinner than 100 μm. A picture confirming this measurement taken with a scanning electron microscope (SEM) (JEOL, Ltd, Akishima, Tokyo, Japan) is shown in Figure 3.7. The SEM also reveals a smooth surface. The two

layers of CNT optimized the balance of thickness and light extinction, while the gold particles helped to reflect and increase the light absorbption further.

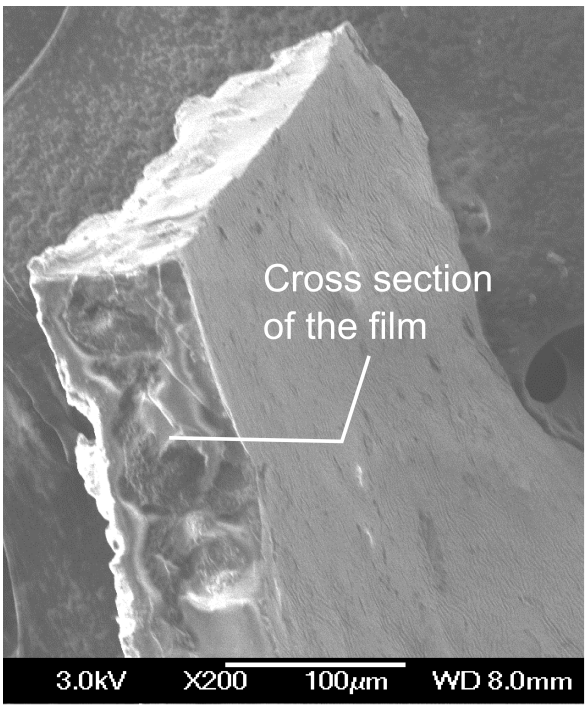

Fig. 3.7 Scanning Electron Microscope image of the light absorbing film.

3.4 Characterization of the transducers

To compare the performance of different substrate materials we limit the study to a single design, i.e. that of a concave spherical shape. The radius of curvature is 10 mm and the opening diameter is 15 mm, which results in a f-number of f/0.67. Figure3.4 shows the illustration and 3D plot of the spherical transducer constructed with the OpenScad (http:// www.openscad.org)(Maintainer: Marius Kintel, Norwegian University of Science

and Technology). The gain factor [3] can be calculated with

$$G = \frac{2\pi f}{c_0} r(1 - \sqrt{1 - \frac{1}{4f_N^2}}) \tag{3.1}$$

which for the present design is $G \approx 200$.

Table 3.2 Material parameters related to the photoacoustic effect

Material	Young's Modulus (GPa)	Optical Transmission (at 532 nm)	Acoustic Impedance (calculated) (MPa.s/m)
Glass	82	92%	11.6
VeroClear	$2.0 \sim 3.0$	86%	1.58
Clear Resin	2.8	87%	1.91
PDMS	0.0013(Agent ratio 1:10) [74]	90%	1.43

Table 3.2 [1] shows some parameters which relate to acoustic and optical properties of the four materials. Optical transmission is measured by exposing the samples of the four materials to a 532 nm laser beam and measuring the transmitted (tested with pulse laser) readings from the power meter (Thorlabs). The four materials show good optical transmission. Their acoustic impedance is approximated from the density of the material and the bulk sound speed. The estimated bulk sound speed was calculated based on the traveling time when the acoustic signal could be detected on the material surface. The acoustic impedance of glass is the highest, while the values of the other three other materials are similar.

The experimental setup to measure the acoustic field generated is illustrated in Figure 3.8. The setup may be separated in two main parts, one part for the photoacoustic wave generation (Part I) and the second part for imaging and monitoring (Part II). The transducer was placed at the bottom of the tank filled with deionized water. Part I contained a high

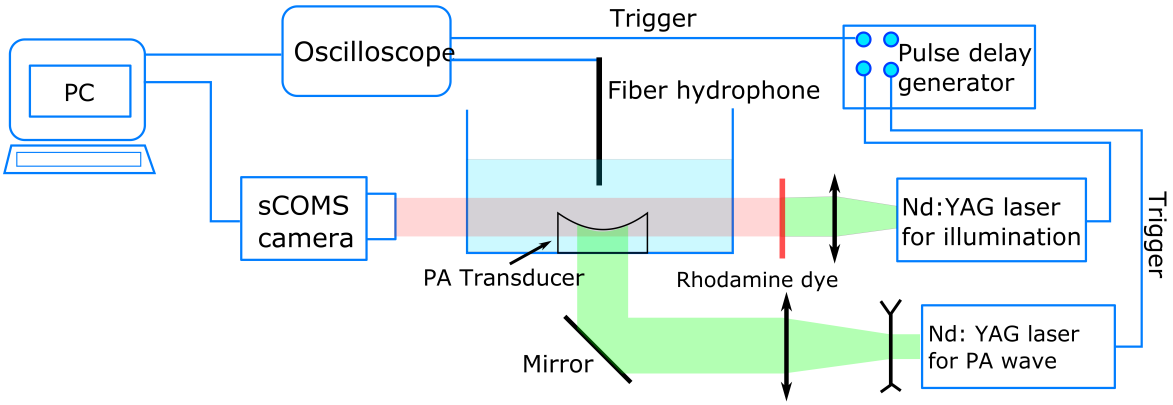

Fig. 3.8 Experimental setup to profile the spherical transducer. Reproduced from [1], with the permission of AIP Publishing.

power laser (Litron Nano Series, Nano L 34010, Q-switch, Nd:YAG laser, λ = 532 nm, pulse width 5 ns), the LGFU transducer and some optics. Part II contains an optical fiber hydrophone (HFO-690, Onda, Sunnyvale, CA, USA), an oscilloscope (Waverunner 64xi, Teledyne, LeCroy, Chestnut Ridge, NY, USA), Rhodamine fluorescence dye (Exciton, LDS 698, Dayton, OH, USA), a Q-switch laser (NewWave Orion, Nd:YAG laser, λ = 532 nm, pulse width 6 ns) and an sCOMS camera with a 10X long working distance objective (Andor Zyla 5.5, Belfast, Northern Ireland and Mitutoyo plan apo infinity corrected long working distance objective, 33.5 mm). The optical fiber hydrophone, which was controlled by a 3D motorized translation stage (Thorlabs, 50 mm, MTS50-Z8), was used to detect the pressure wave coming from the transducer. The bandwidth of the hydrophone is between 3 kHz and 150 MHz. The laser was used for illuminating the region of interest (area of the diameter of 1 cm). The experiment is triggered by a pulse delay generator (BNC 575, Berkley Nucleonics Corporation, San Rafael, CA, USA) controlling the laser, the cameras, and the trigger of the oscilloscope.

First the pressure maximum was found by scanning the fiber hydrophone through the acoustic pressure field emitted by the transducers. For each value of the laser energy setting, 10 measurements were recorded and plotted with the standard deviation as error bars, see Figure 3.9. In low laser fluence region, the pressure amplitudes do not differ significantly, while large difference of values appear beyond 4 mJ/cm^2. The glass and resin responded similarly to the laser input, meanwhile PDMS and VeroClear showed 30% and 45% lower pressure amplitudes.

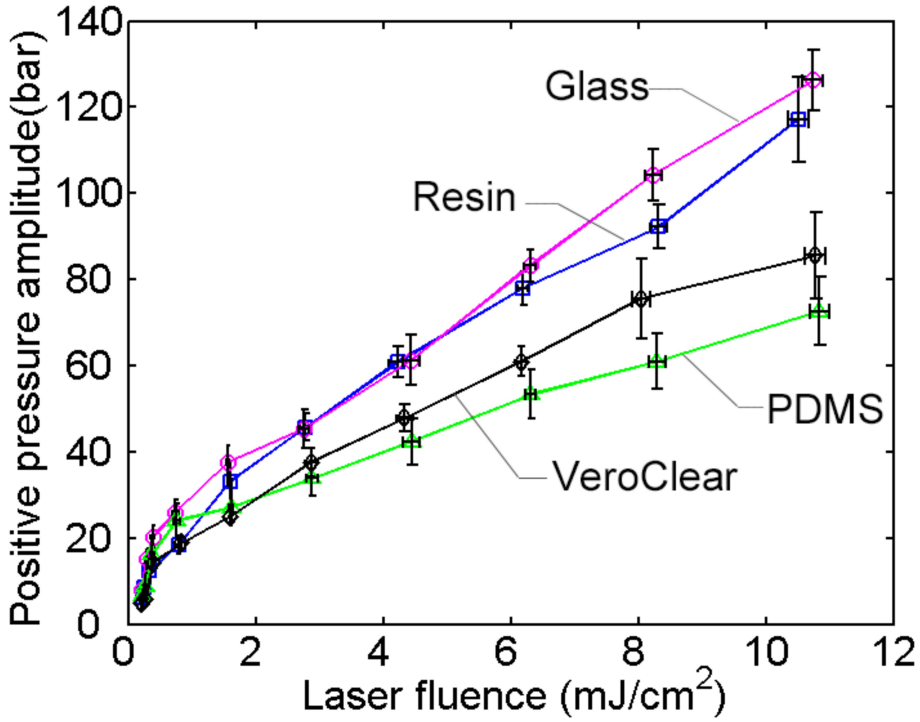

Fig. 3.9 Positive pressure amplitude versus laser fluence of the four susbtrate materials. Reproduced from [1], with the permission of AIP Publishing.

We also measured the profiles of the acoustic pressure along the central axis of the four transducers, as shown in Figure 3.10. The laser input was 10 ± 0.15mJ/cm^2. As the results PDMS and VeroClear show considerably lower amplitudes as compared to glass and

resin substrates, i.e. their readings is nearly half of that latter ones. Next we focus on the comparison between glass and resin substrates. The clear resin transducer has a similar performance as the glass transducers for the positive pressure vales and which may reach above 100 bar. Yet, their is a significant difference for the negative pressure. The glass substrate results in nearly three times lower negative pressure than the clear resin substrate. The axial length FWHM of the pressure distribution is about 1 mm.

Figure 3.12 compares the spatial pressure distribution through contour plots of the clear resin substrate (left) with the glass substrate (right). For this the scan area of the fiber hydrophone is set to $\times 1\,\mathrm{mm}^2$ with a step size of $50\,\mu$m. The measurement has been automated using a motorized translation stage (Thorlabs, 50 mm, MTS50-Z8), procedures as shown in Figure 3.11. The focal plane was divided into small step. The hydrophone was driven to the each point on the map under the control of the motorized stage. Measurements were taken upon arrival of the fiber probe. Once finished, the probe moved to the next point. Under ideal conditions the pressure distribution should be axial symmetric, yet imperfection of the transducer and likely also for the measurements result in some non-asymmetric contours. The full width at half maximum (FWHM) of the peak pressure is about 250 μm for the resin substrate, while it is $400\,\mu$m for the glass substrate. The high pressure region from the clear resin is concentrated within an area less than $250 \times 250\,\mu\mathrm{m}^2$ which is of the order of the size of the fiber diameter of 125 μm.

We find that the pressure wave emitted from the resin transducer shows a considerably faster rising time of 20 ns and the signal of the positive pulse is followed by a larger negative tail with the amplitude similar to the positive part, as compared to the transducer of the

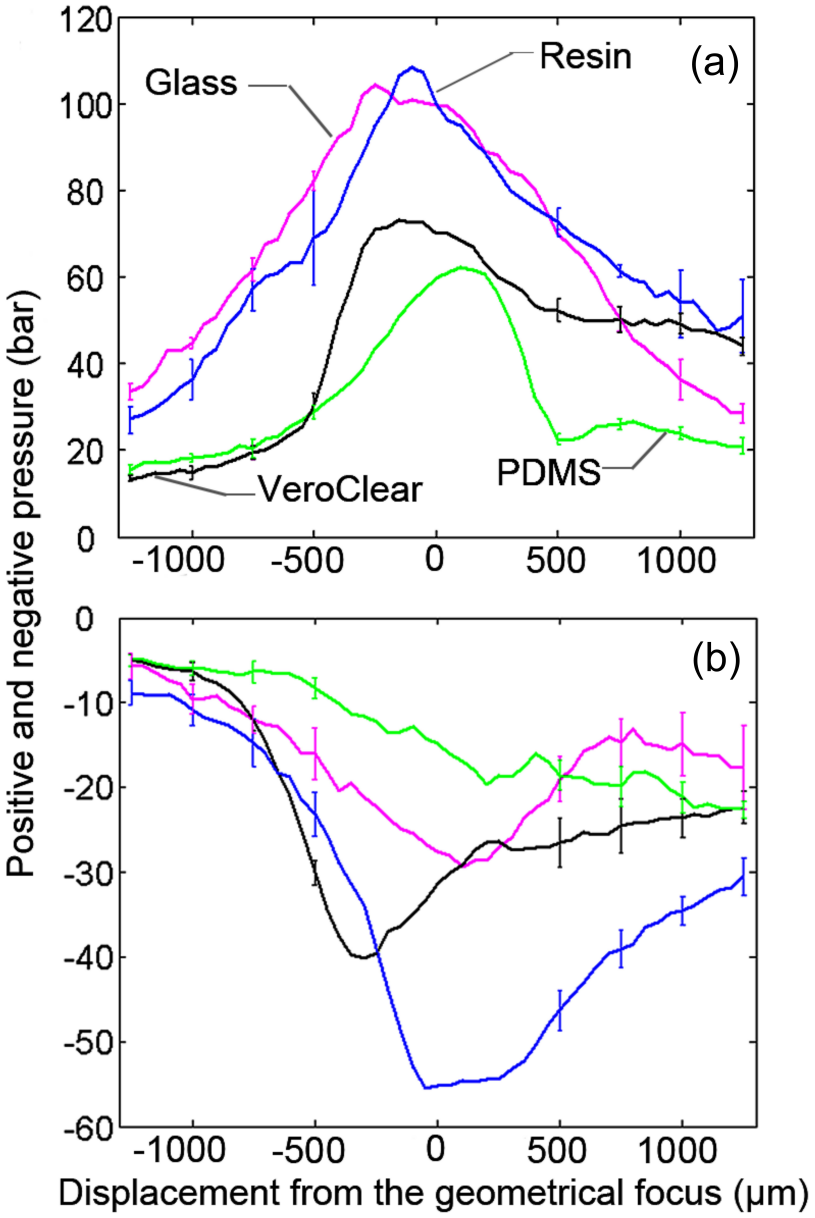

Fig. 3.10 The pressure distribution along the central axis of the transducer of the spherical transducer of the four materials (at 10 mJ/cm^2). (a) shows the positive pressure, and (b) the negative pressure. Reproduced from [1], with the permission of AIP Publishing.

glass substrate as in Figure 3.13(a). This is also evident in the frequency spectrum of both waves shown in Figure 3.13(b). Both spectra were normalized to the maximum amplitude

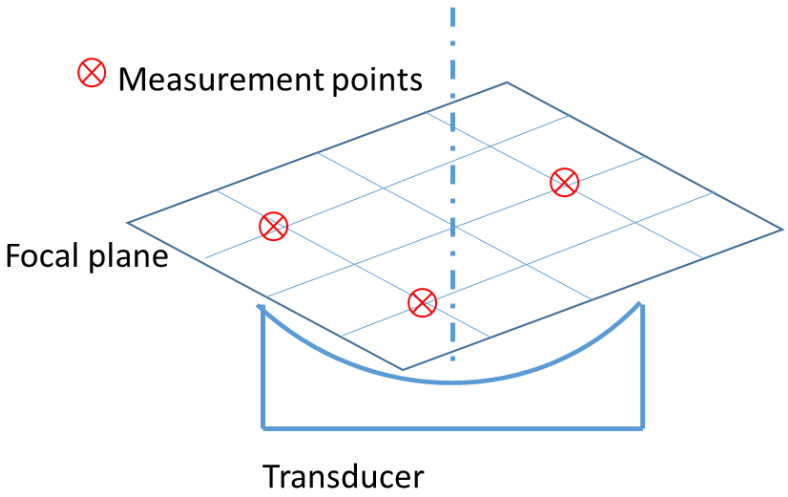

Fig. 3.11 Methodology to scan pressure distribution in the horizontal focal plane.

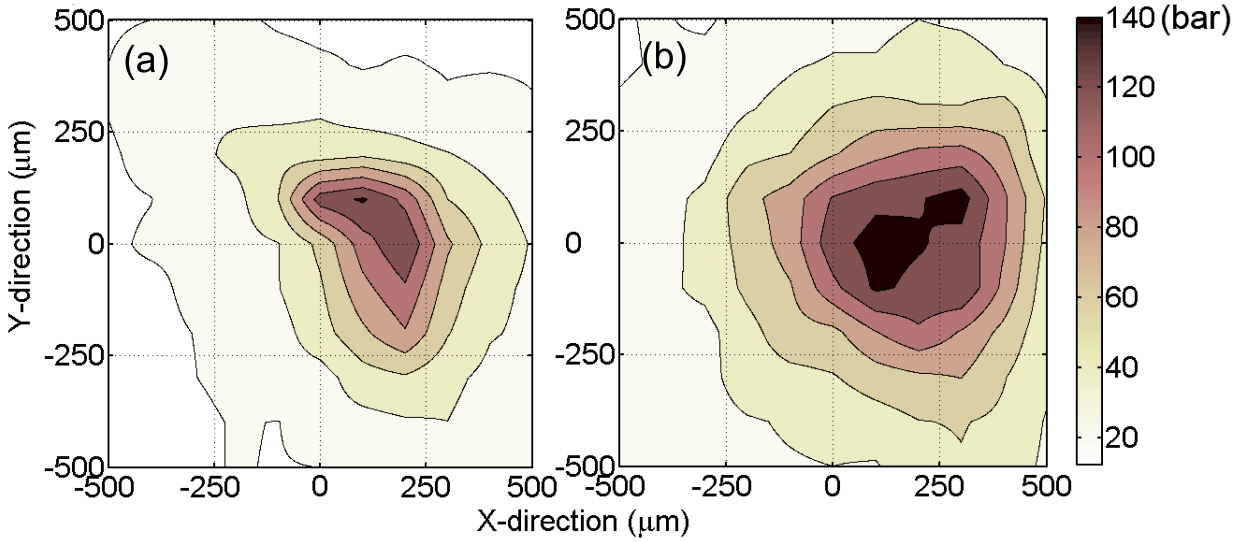

Fig. 3.12 Positive pressure distribution in the horizontal focal plane from the resin (a) and the glass (b) substrate. Reproduced from [1], with the permission of AIP Publishing.

of pressure from the transducer of the glass substrate, i.e., the maximum amplitude of the glass substrate is taken as the reference pressure when calculating the frequency spectra. The frequency spectrum is calculated by using the function of fast Fourier transform. The maximum frequency of the glass is about 6.7 MHz, while the resin shows about 8.3 MHz.

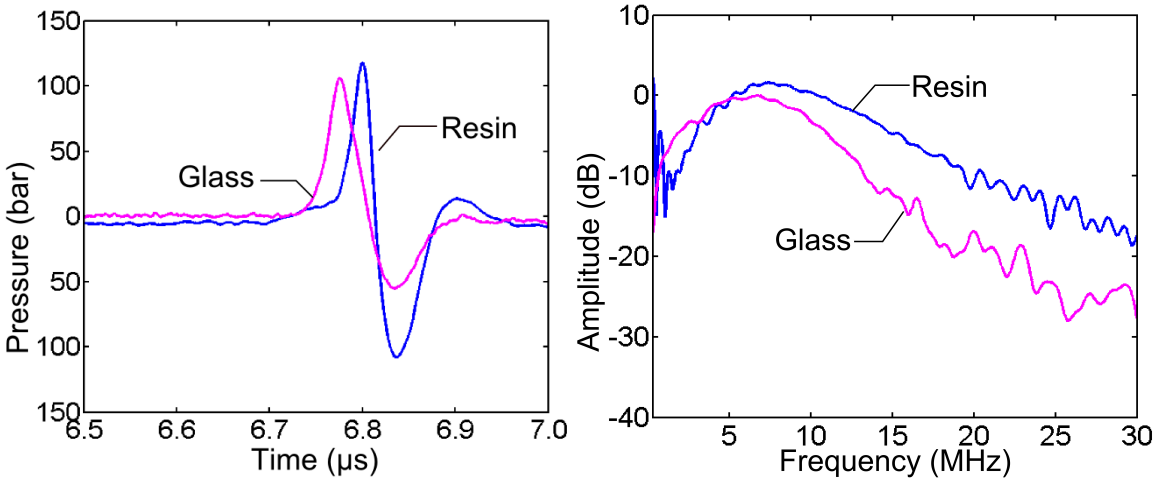

Fig. 3.13 (a) The pressure measurement at the focus; (b) the frequency spectra from the glass and the resin substrates, normalized to the maximum amplitude of the glass substrate. Reproduced from [1], with the permission of AIP Publishing.

The difference between the experimental frequency and the theoretical frequency should be attributed to the thickness and the size of the light absorbing material particle or cluster [33].

By simple physical deposition allows to fabricate a thin light absorbing material on the hard surface suitable for photoacoustic wave generation. By characterizing the four light absorbing materials and several substrate materials, we obtained a suitable combination of coating and substrate material. This combination will be used in the latter chapters for the transducer designs. The transducer made of CNT-PDMS mixture layer and clear resin by the 3D printer shows a comparable performance as the glass substrate.

Chapter 4

Realization of arbitrary wavefront by the 3D printer and other fabrication approaches

4.1 Introduction

Upon finding a good combination of coating and substrate material, we want now to utilize the capabilities of 3D printing to design more complex geometries of the transducer. Basically, the surface of the transducer launches elementary waves very similar to a phase hologram used in optics [75]. The measurements are compared with simulations of the wave field. Besides more complex waveforms we also were interested in increasing the peak pressure. We achieved by increasing the gain factor pressures of up to 500 bar in amplitude without damaging the substrate and coating. The transducer may not always need to be coupled

through water but can be directly attached to a glass plate to focus the acoustic energy into microchannels for lab-on-a-chip applications.

4.2 Different designs of the transducers

Due to the short turn-around time between design and having the product, 3D printers are versatile for producing customized geometries. We started with a design goal to generate a transducer, which generated two separated waves separated in time. With a sped of sound in water of 1500 m/s and typical substrate sizes of 1 cm an effective delay is limited to about $5-6\,\mu$s. In our specific design we a two stepped design, where the outer surface has a radius of curvature of 10.0 mm and the inner surface a curvature of 11.2 mm. As the inner surface is lowered by 1.2 mm, both foci are at the same location as shown in Figure 4.1. This design is aimed to generate two wavefronts with the temporal spacing of $0.8\,\mu$s. We conducted the experiment by using the same setup as shown in Figure 3.8 with the stepped photoacoustic transducer. This time we ran the input laser at 8 mJ/pulse (in a circular area of diameter $\sim$10 mm).

Figure 4.2 shows the hydrophone reading with two pulses separated 0.8μs in time. The amplitude of the first pulse is about 5 times stronger than the amplitude of the second. Both of their negative pressure amplitudes are slightly smaller, about 80% of the positive amplitude. The shape of the wavefront becomes evident from the shadowgraph images taken with a sCMOS camera (Zyla sCMOS Camera, Andor, Belfast) and pulsed laser illumination. Here, figure 4.6(a) reveals two wavefronts separated in a space by approx. 1.0 mm. Interestingly,

the first wavefront shows the expected focus of a spherical wave front while the trailing pressure wave resembles a planar wave. This is at first unexpected, as the structure has two curved parts which should lead to two spherical wavefronts. We explain the discrepancy that the milder curvature is further "flattened" by the coating, which then leads to an almost flat surface which launches an almost planar wave.

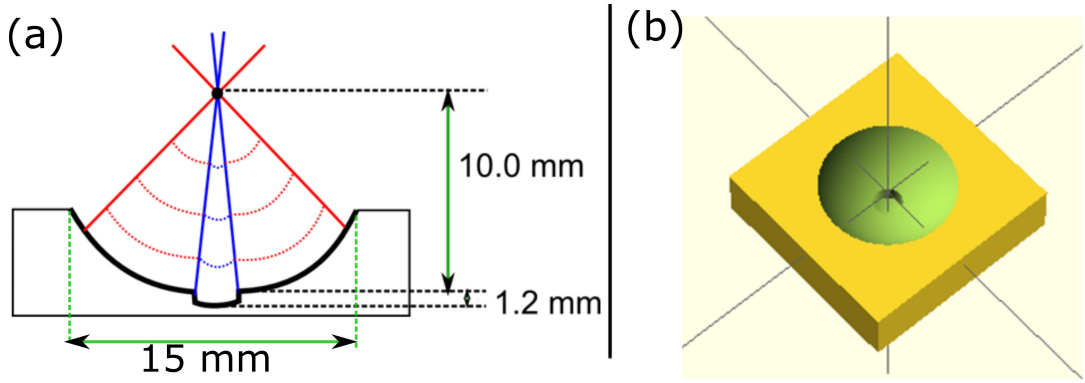

Fig. 4.1 Illustration of the the two stepped transducer: (a) 2D plot and (b) 3D model.

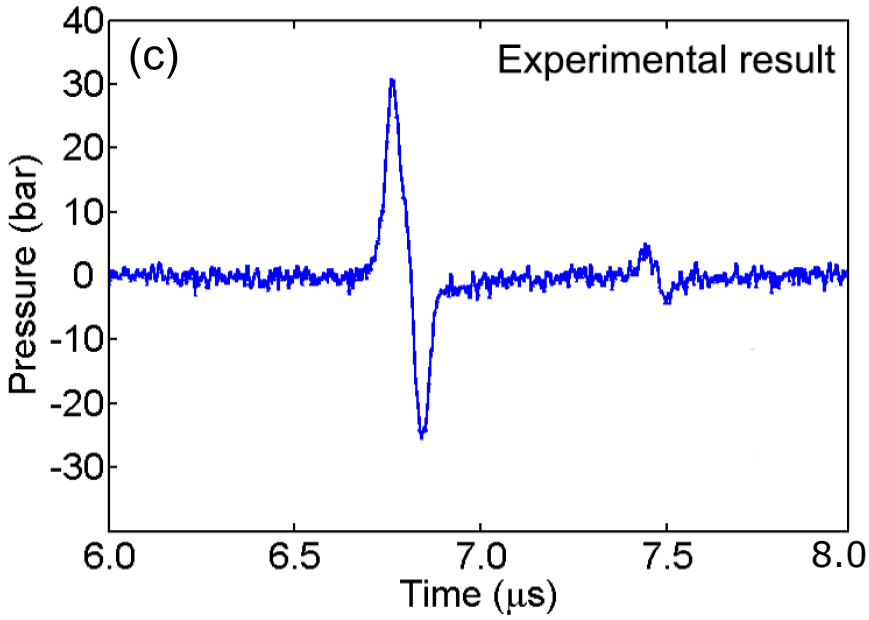

Fig. 4.2 Pressure reading from the two-stepped transducer.

Another design able to generate a two-peaked pressure signal is a cross-stepped transducer as presented in Figure 4.4(a). The upper and lower surface have the same surface area, thus one expects to generate peaks of similar amplitude. The measured pressure at their combined focus is shown in Figure 4.4(b). Here the trailing pressure signal is about 80% larger than the leading amplitude. We find also largely different negative pressure signals. The complex shape of the pressure signal is likely caused by diffraction waves from the edges of the structure and the 3-dimensionality of the surface.

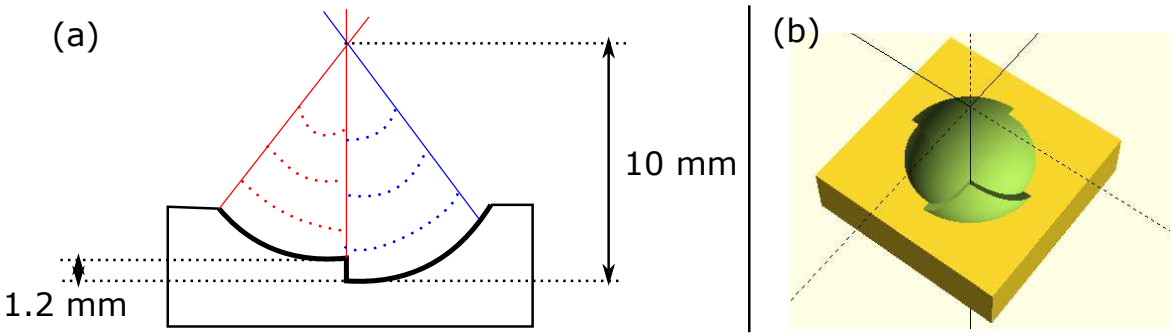

Fig. 4.3 Illustration of the cross step transducer: (a) 2D plot and (b) 3D model.

4.3 Simulation of the pressure from structured transducers

Next we want to calculate the waveforms emitted. For this we ignore the mechanism of wave generation and start with few cycle harmonic wave enveloped by Gaussian. Also to reduce memory consumption we only study axisymmetric propagation, thus we cannot compare the wave generated from the cross-stepped transducer. We further assume that the pressure

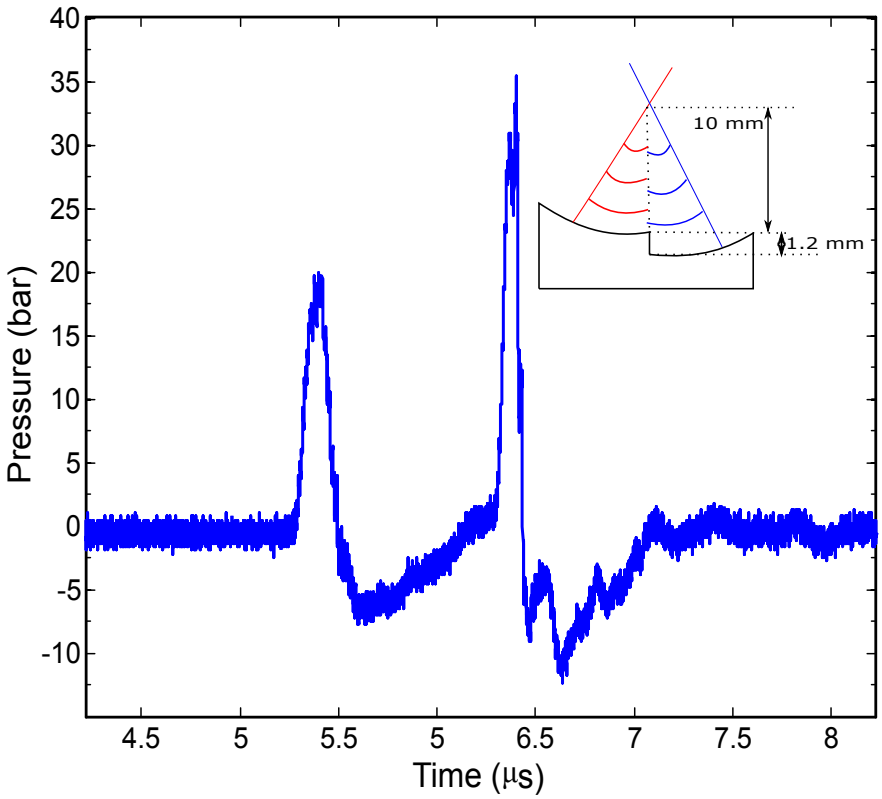

Fig. 4.4 Pressure measurements of the cross transducer.

amplitude generated is proportional to the absorbed laser energy, thus to the projected surface area exposed to the laser beam, see Figure 4.5.

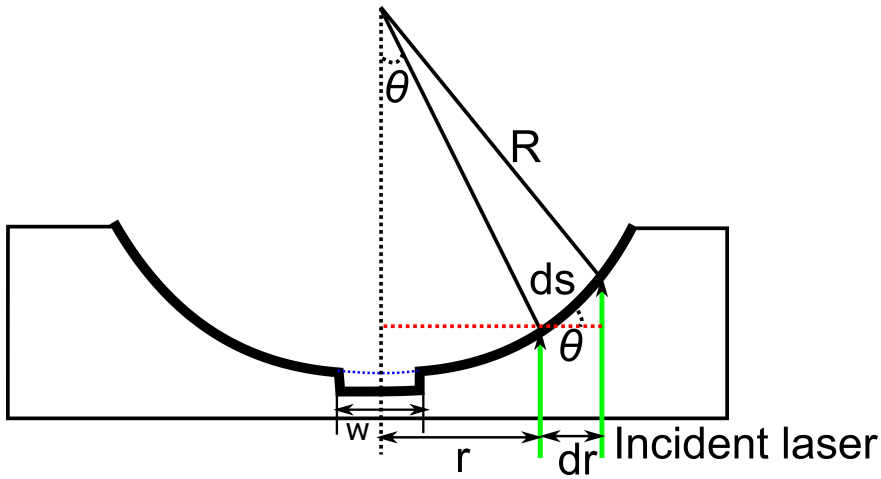

Fig. 4.5 Simplified geometry of the two-stepped transuducer.

In Figure 4.5, r is the radial distance from the axis of symmetry, R is the radius of curvature, w is the diameter of the lower stepped structure, and θ is the angle between the vertical central axis and the selected surface element. In our geometry $R = 10\ mm$ and $w = 4.0\ mm$. The projected area of the lower level is

$$A_{lower} = \pi(\frac{w}{2})^2 \tag{4.1}$$

The projected area of the spherical surface is

$$dA_{arc} = ds \times 2\pi \times r \tag{4.2}$$

and the energy absorbed is as

$$P_{arc} \propto dA_{ver} = dr \times 2\pi \times r \tag{4.3}$$

Approximately, we have for

$$cos\theta = \frac{dr}{ds} \tag{4.4}$$

and

$$sin\theta = \frac{r}{R}. \tag{4.5}$$

small θ. Thus,

$$(\frac{dr}{ds})^2 + (\frac{r}{R})^2 = 1 \tag{4.6}$$

We solve for

$$ds = \sqrt{\frac{1}{1-(\frac{r}{R})^2}}dr \tag{4.7}$$

Due to the proportionality of absorbed energy and the area,

$$\frac{P_f}{P_{projection}} \propto \frac{dr \times 2\pi \times r}{ds \times 2\pi \times r} = \sqrt{1-(\frac{r}{R})^2} \tag{4.8}$$

and

$$P_{planar} = P_0 \times A \tag{4.9}$$

To compare the stepped transducer we use the geometry from the design files, except for the lower surface we assume a plane due to the reasons explained above.

The calculation is also based on the simplification of a linear wave model, i.e.

$$\frac{\partial^2 u}{\partial t^2} = c^2 \frac{\partial^2 s}{\partial t^2} \tag{4.10}$$

the nonlinearity of the wave is not revealed by the calculation results. The differential equation is solved in the axial symmetrical coordinate. We implement the geometry from the experiment and obey the Courant-Friedrich-Levey condition for convergence of 0.7 when simulating by COMSOL (COMSOL, Inc. Burlington, MA, USA). By taking use of the partial differential equation in COMSOL, we set the boundary as the hard wall, and the initial velocity of the wave was 0. The filled liquid is water of density 1000 kg/m^3 and sound velocity as 1480 m/s in water.

Figure 4.6 compares the shape of the wavefronts obtained with shadowgraphy with the simulation results. The shadowgraphy shows contrast at locations of a large magnitude in the the second spatial derivative of the index of refraction [76]. The index of refraction is proportional to the pressure through the Gladstone-Dale relation [77], thus the shadowgraph in Figure 4.6(a) shows locations of large second order derivatives of the spatial pressure distribution.

For the simulation results, Figure 4.6(b), the red color represents positive values, whereas the blue color represents negative values. After the pressure wave hits the tip of the fiber, a clear diffraction wave was observed leading to the creating of a strong negative pressures. This is important for the later results shown in section 5.6. In Figure 4.7 and 4.6, the signal from the hydrophone and the calculation results are consistent, which reveals the time delay of the two wavefronts is consistent with the geometry of the transducer. From the calculation, it is also possible for us to find out the wave propagation near the surface od the transducer, which cannot be observed from the camera, as in Figure 4.10. The deformation of the wave from the corner cannot be avoided in the real case. We can see clearly the scattering wavefronts near the corner of the bottom from the calculation. Actually, the corner effect is inevitable. In the fabrication, it is not easy to cover the corner with the light absorbing material because of the shape structure. Thus, light leakage will be caused by the sharp corner, which may lead to lower pressure values compared with the spherical case. The first peak was around 40 bar and the second peak was 10 bar.

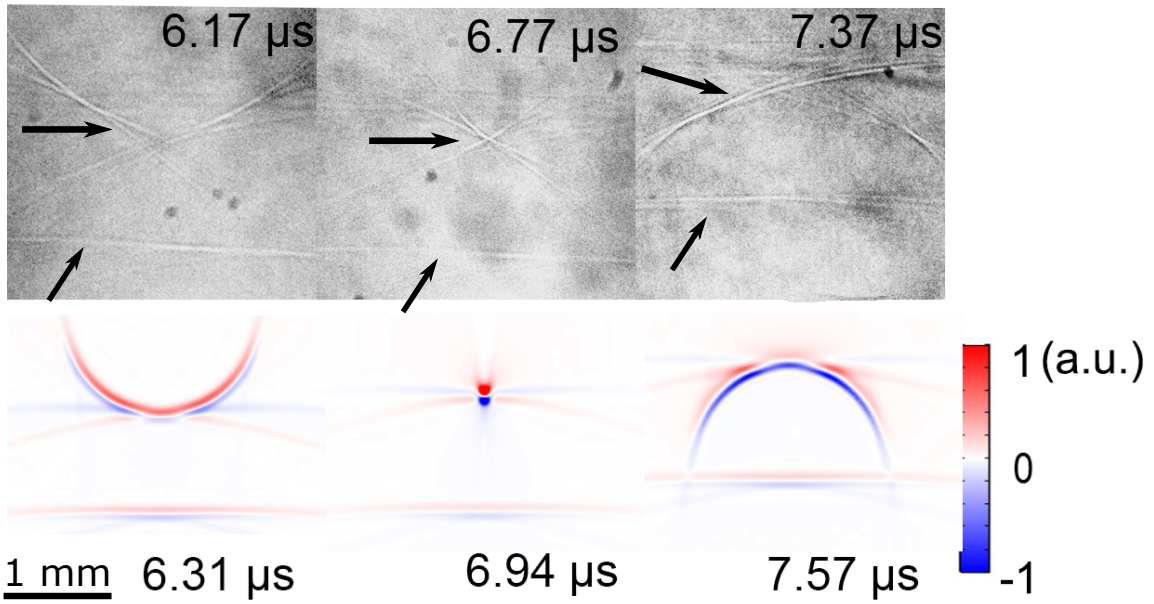

Fig. 4.6 Comparison betweent the real experiment and the simulation (without fiber) . The arrows denote the wavefronts.

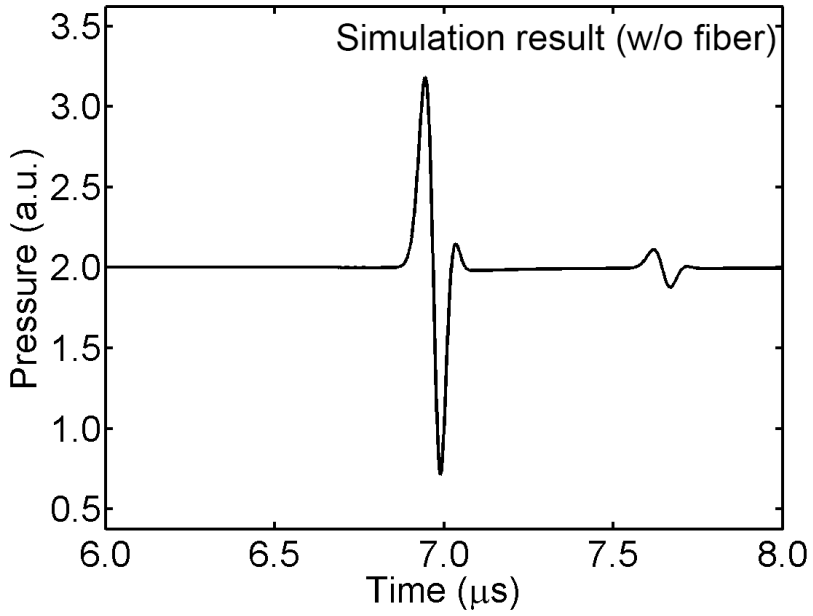

Fig. 4.7 Reading from the probe near the focus without placing the fiber.

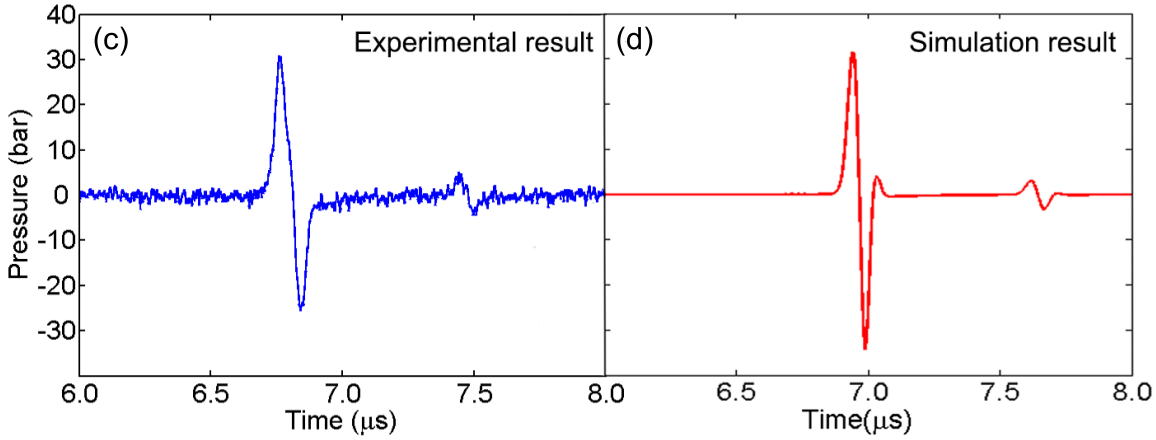

Fig. 4.8 Reading from the probe near the focus with placing the fiber.

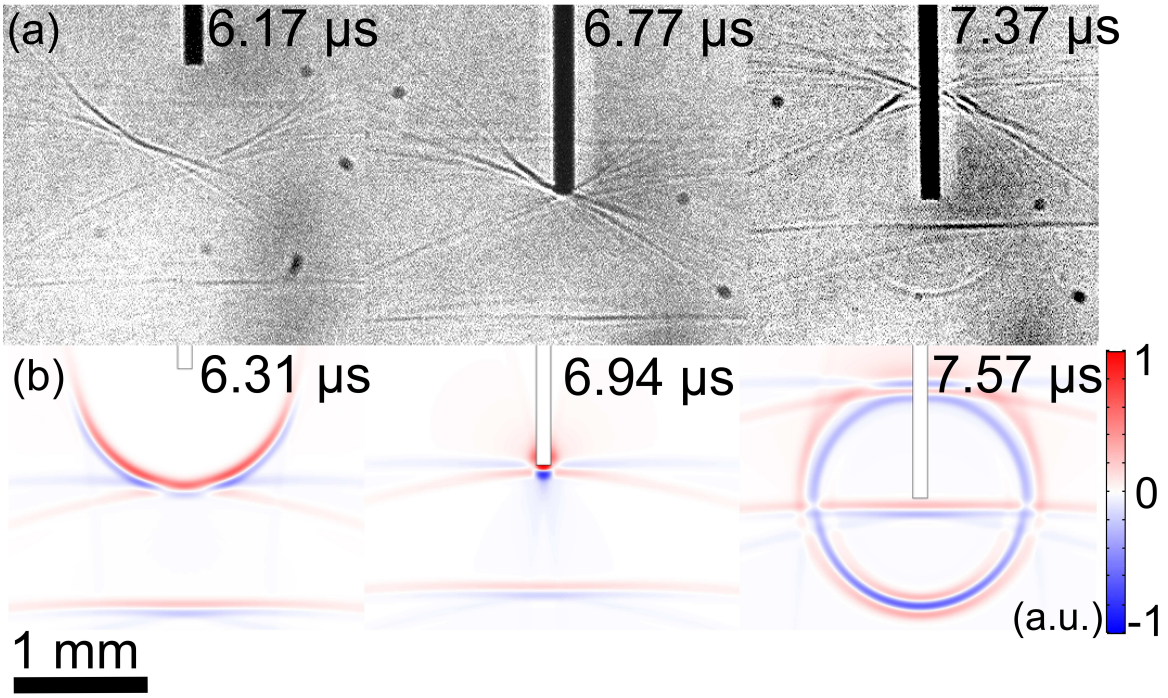

Fig. 4.9 Comparison betweent the real experiment and the simulation (with fiber).

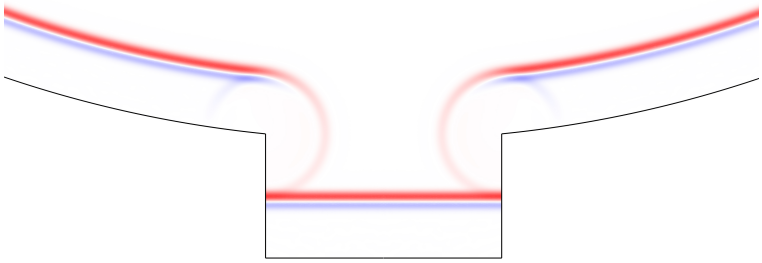

Fig. 4.10 Diffraction wave at the corner from calculation.

4.4 Towards generating higher acoustic pressure

In order to achieve higher acoustic pressure for both peaks, we realized that the laser energy and light absorbing efficiency should be improved. Therefore, we made effort in more consistent coatings, increasing the laser energy, increasing the gain factors and changing the settings for the 3D printer.

The numerical aperture/opening angle is an important parameter for the gain, see Eq.2.3. We therefore redesigned the geometry of the transducer. Our aim was to increase r and f_N. First, changes were made on the spherical transducer. The opening of the transducer was increased twice larger, i.e., 3.0 cm as in Figure 4.11, in order to reduce the escape of light from rim of the top. The curvature was also deeper to 2 mm. By this setting, the gain factor was increased from 100 to 300, based on Eq.2.3, see [3]. The input energy from the laser was tuned to 16 mJ/pulse, which was the maximum output of the current laser. The

printing setting of the resin supporter for the substrate was changed to reduce the roughness of the inner bottom surface. The setting may lead to increase of printing job failure, but do benefit smoothening the surface. The maximum pressure of the first peak was over 500 bar, which has been improved nearly 5 times from previous setting, as shown in Figure 4.12. While, the amplitude of the negative pressure was also increased, but less, around twice. The difference between the amplitudes of positive and negative parts were further increased. The high positive pressure provides the compulsory experimental condition for the experiments in Chapter 5.

Upon the improvement on the spherical transducer, the performance of the two-stepped transducer can also be enhanced by the same method. The change of the geometry was made as in Figure 4.11(a). This time, the two pressure peaks experienced a great increase to nearly 500 bar and -100 bar. This should be attributed to the enlarged stepped structure, as it reduced difficulty of painting. Here, we increased the step size of the geometry to 2 mm to compromise to better painting. Furthermore, the corner was polished more smooth but not a sharp hump. By these tricks, painting of the light absorbing material was easier to handle and the leakage of laser light was reduced at the corner.

4.5 Alternative approaches to photoacoustic transducers

Although the stereolithography printer (Formlabs, Somerville, Massachusetts, United States) can provide good quality of the transducer, the waiting time takes hours after optimizing the printing setting. Meanwhile, the failure rate of the print jobs is a considerable factor.

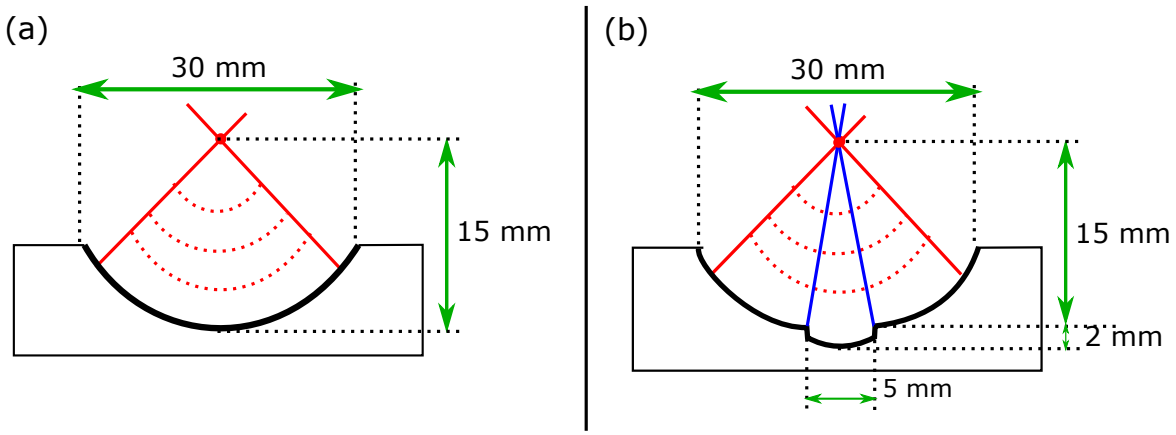

Fig. 4.11 Illustration of the improved transducer to increase the pressure. (a) Spherical transducer; (b) two-stepped transducer.

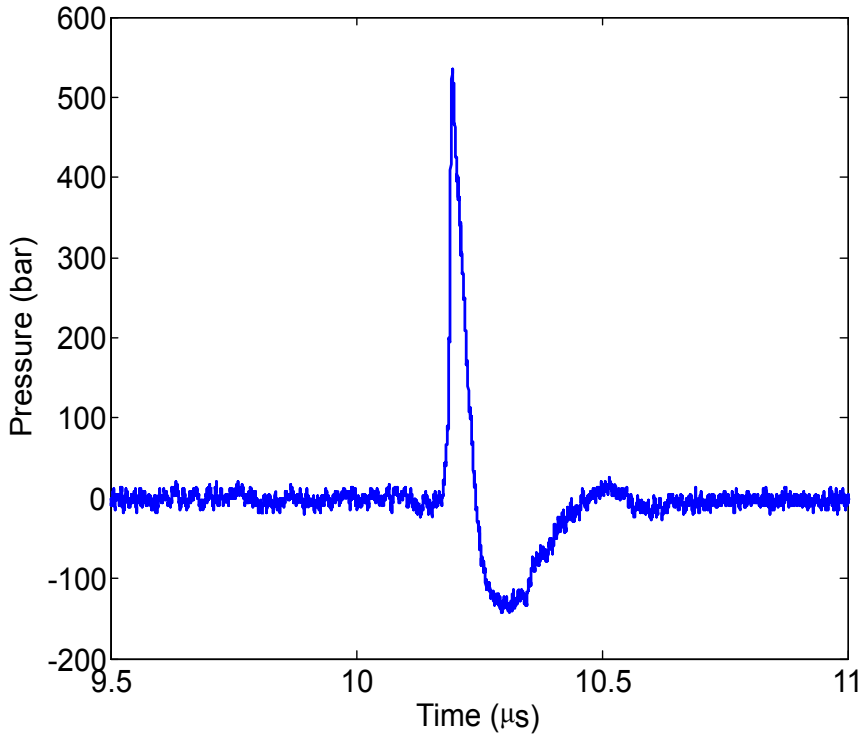

Fig. 4.12 Pressure reading from the improved spherical transducer.

Therefore, besides direct utilization of 3D printers to fabricate the photoacoustic transducer substrates, several flexible and simple methods were also developed. In this section, transducers made by two methods are introduced: PDMS casting transducer and droplet transducer.

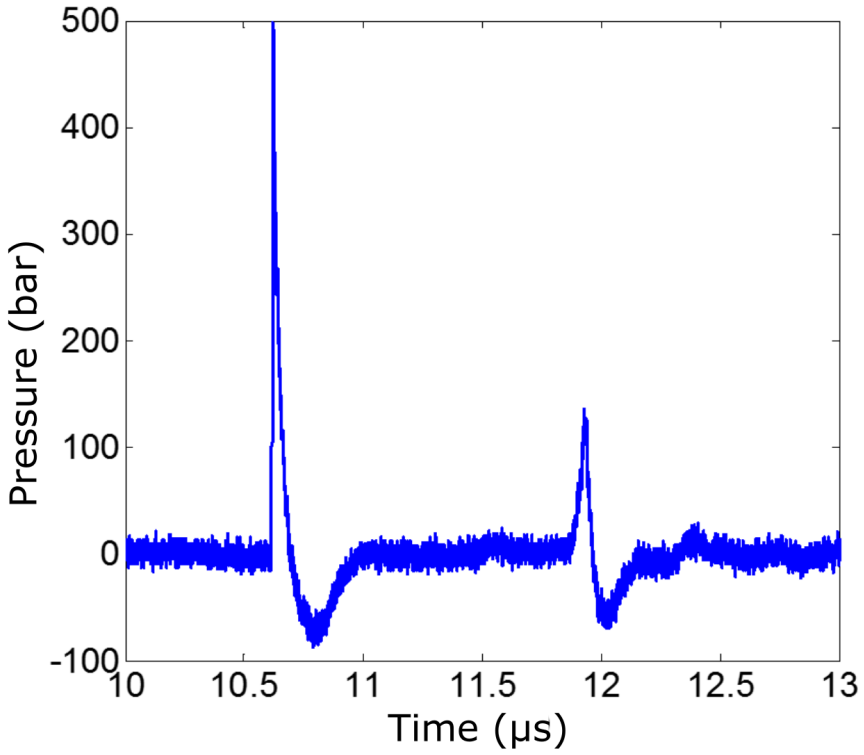

Fig. 4.13 Pressure reading from the improved two-stepped transducer.

These two methods are of lower cost, less time consuming and able to achieve minimal structures suitable for multi-time usage. With the two methods, the transducers can still achieve a high spatial resolution. However, meanwhile, compromise has to be made in getting higher pressures, which is lower than 60 bar in measurement. The gain factor of the droplet transducer is ∼57, which is smaller than normal size transducer. In real measurement, the value was even lower. In the experiment, we found that by using these methods, the light absorbing cannot bear higher laser input energy over 8 mJ/pulse. The light absorbing film was immediately damaged if being exposed under higher laser fluence (∼0.16 mJ/mm^2). In the case of PDMS casting transducer, the pressure was found to be relevant with the PDMS-agent ratio.

4.5.1 PDMS casting transducer

So far the transducer substrate was directly printed, yet it is also possible to combine 3D printing and PDMS casting to fabricate transducers. For this we utilized a filament based 3D printer (Ultimaker 2.0, Geldermalsen, Netherlands) to print the negative mold for PDMS casting using a PLA filament.

The procedures are demonstrated in Figure 4.14. First we printed the negative mold and cleaned the surface by wiping it with ethanol. The percentage of printing material filling was set to 100% to make the inner structure dense, in order to avoid trapping air from inside the mold during the degassing of the uncured PDMS. A scotch tape was sticked to the four sides of the mold leaving a rim of about 2 mm above the hemisphere. Before heat curing PDMS it must be degassed to remove the air bubbles which eventually become entrained during the mixing with the curing agent. Then the degassed PDMS was poured into the mold and sent to cure for 1 hour in the oven. The cured PDMS could be peeled off the mold and is painted with the CNT-PDMS mixture. The negative mold can be used for multiple times after proper cleaning with ethanol in an ultrasonic water bath. In general, casting a transducer is typically faster than printing as the chance of a false print is avoided.

The dimension of the transducer followed the setting (The radius of curvature is 10 mm and the opening diameter is 15 mm) in Chapter 3. Samples of transducers are shown in Figure 4.15. PDMS remains liquid under room temperature without a curing agent. We tested if the ratio between PDMS and curing agent determines the performance of the transducer. It has been reported that the Young's modulus of cured PDMS is strongly affected by this ratio [78]. We tested the ratios 5:1, 10:1, and 15:1. The ratio 15:1 and below did not allow curing of the

PDMS, while the ratio 5:1 and 10:1 lead to working transducers. The resulting pressure wave forms are shown in Figure 4.16. The PDMS with the higher curing agent content resulted into an approx. 30% larger positive peak pressure as compared to the softer PDMS at 10:1.

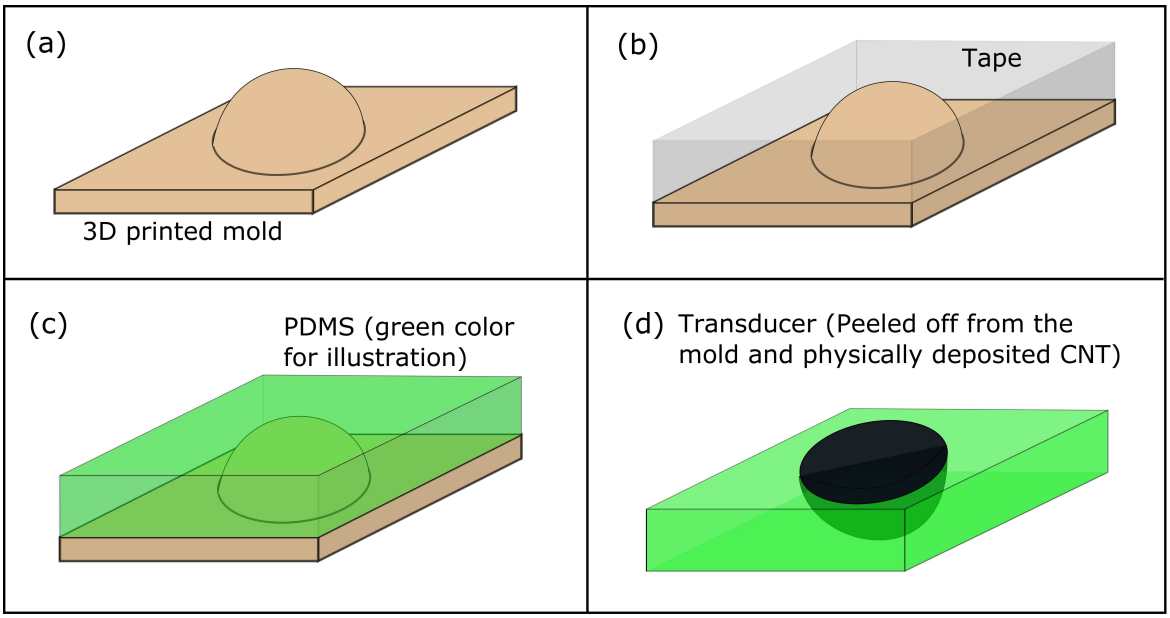

Fig. 4.14 Procedures to fabricate the transducer.

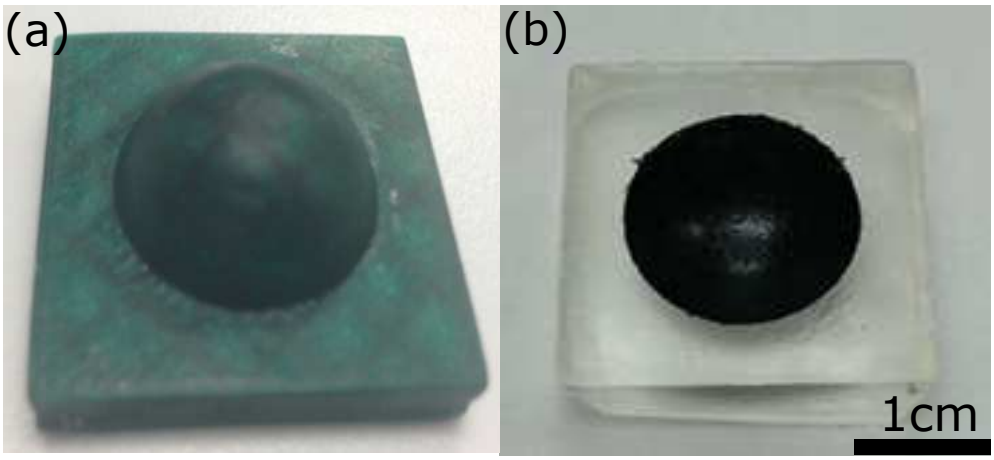

Fig. 4.15 (a) PLA negative molds from Ultimaker and (b) PDMS casting transducer.

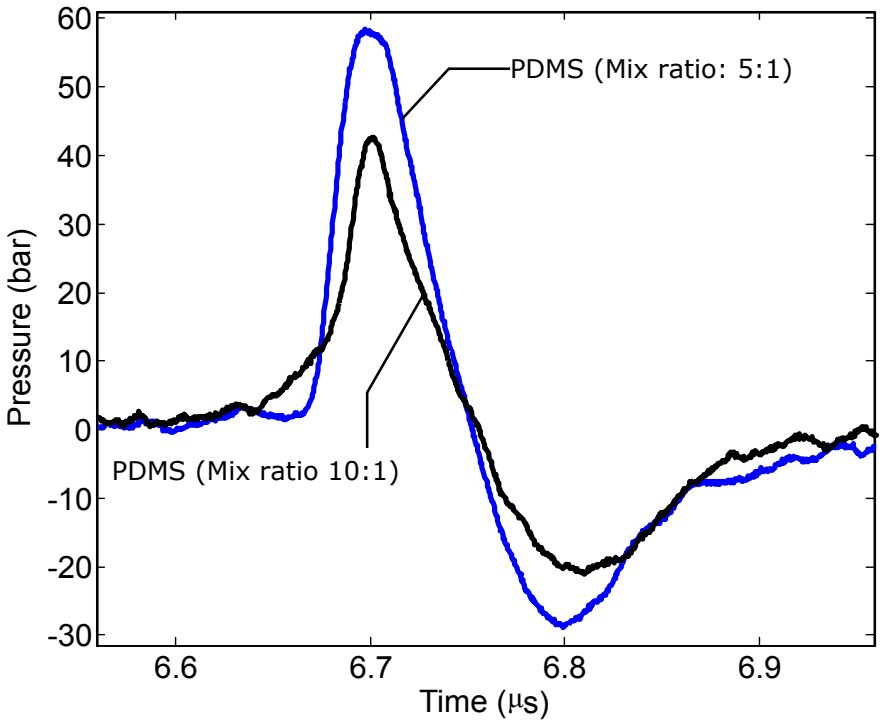

Fig. 4.16 Pressure measurements for the PDMS casting transducers of different mixture ratio (5:1 and 10:1, at the same laser exposure energy, ∼8 mJ/pulse).

4.5.2 Droplet-based transducer

Previous research [79] has demonstrated a surprisingly simple technique to build optical lenses from curing drops of PDMS on glass. This method may be also allow to fabricate transducer which focus acoustic waves close to a substrate, for example in a Lab-on-a-Chip application. We combined the lens formation with the direct painting of the light absorbing coating to study a droplet-based transducer.

The glass plate was first cleaned with acetone and ethanol to remove the dust on the surface and dry blown with nitrogen gas. PDMS was mixed with the curing agent (Sylgard 184, polymer to curring ratio is 10:1) and degassed before using. Fabrication procedures are shown in Figure 4.17. One drop (∼200 μL) of degassed PDMS was dropped on the

glass plate with dimensions of 50 mm $\times$ 70 mm $\times$ 1 mm (Microscope slides from Fisher Scientific). After the droplet spread to a size of about 1.5 cm in diameter, the glass plate was quickly flipped and hang over such that gravity pulled on the droplet. After 30 minutes upside-down at room temperature some of the PDMS dropped from the glass and a fixed shape of the drop was obtained . The droplet transducer was taken to cure in 80∘C hot oven for 30 minutes. The conventional fabrication process of the light absorbing surface was applied on the cured droplet transducer. By this method, the size of the transducer can be reduced to about 1 cm in diameter with the radius of curvature of millimeter level no more than 5 mm, thus resulting to a focus very close to the glass plate's surface.

The droplet transducer was placed in the tank filled with deionized water. The hydrophone was placed 1 mm over the glass surface to measure the pressure. From the reading of the oscilloscope, the pressure from the droplet transducer could reach over 40 bar, as shown in Figure 4.18. The high pressure area is concentrated tightly within the range less than 500 $\times$ 500 μm^2 at the energy input of 8 mJ/pulse of a beam of size 1.0 cm in diameter, as shown in the contour of Figure 4.20. Compared with the normal spherical transducer, the wavefront still keeps consistent performance in spatial profile with the FWHM of 500 μm, but slower rising time of 400 ns. The pressure attenuates with the displacement from the surface of the glass plate, shown in Figure 4.19, which indicates that the high pressure was focused very near to the surface. However, in the experiment, we found that by this method, the light absorbing film could not bear higher energy input beyond 8 mJ/pulse, otherwise the film was burnt, deformed and failed to perform normally. The damage threshold in this case was lower than the transducers with substrate, which could bear the pulse of

∼16mJ/pulse. The reason for the damage may be claimed that there is no supporting material beneath the film diffusing the incident light. Therefore, the direct exposure caused the sudden high energy concentration which exceeded the damage threshold of the film.

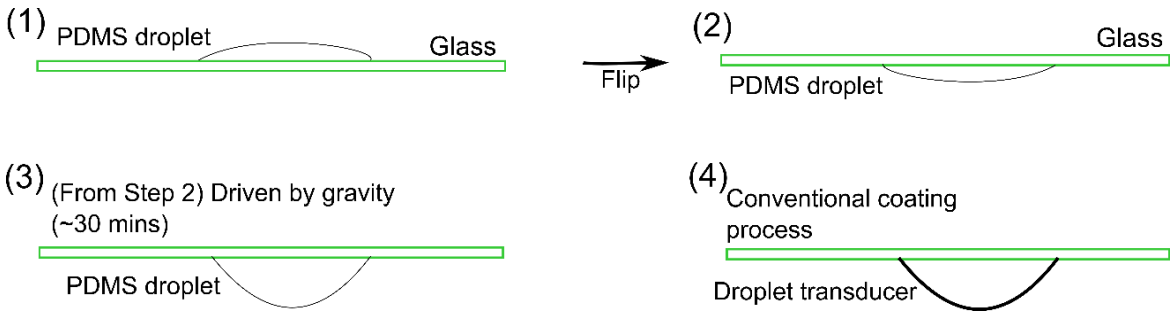

Fig. 4.17 Procedures to make the droplet transducer.

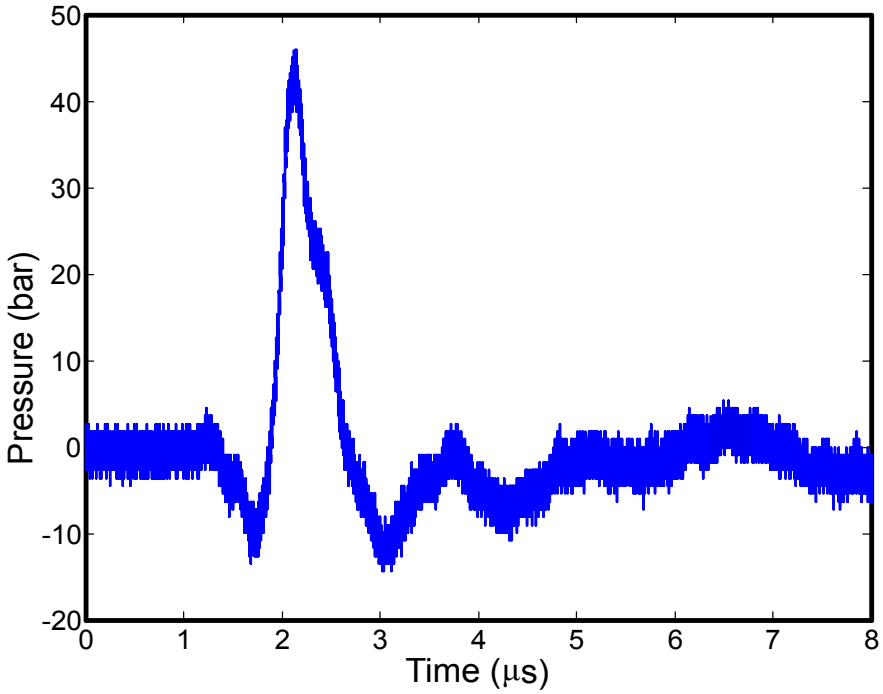

Fig. 4.18 The signal of the hydrophone from the droplet transducer.

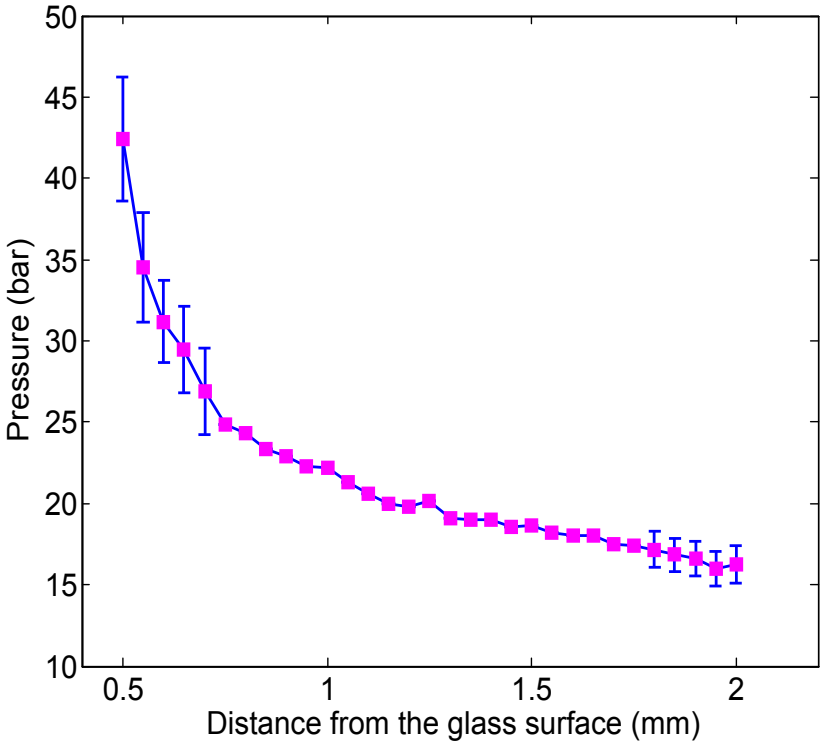

Fig. 4.19 Positive pressure measurements along the vertical direction away from the glass surface, where the errorbar indicates the standard deviation values from the scanning readings.

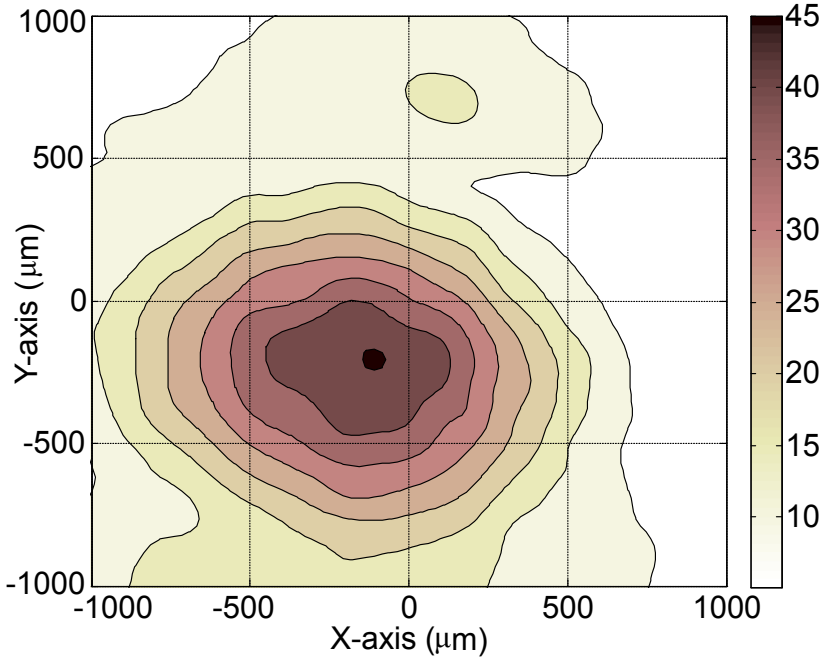

Fig. 4.20 The pressure distribution contour in the focal plane.

Chapter 5

Interfacial cavitations induced by photoacoustic shockwave

5.1 Introduction

The photoacoustic shockwave shares the properties of all acoustic shockwaves, namely high frequency, high amplitude and nonlinearity [3, 16]. An initial aim of the studies was to rupture the liquid through cavitation from the photoacoustic generated shock wave. Recently, Lee et al. [39] demonstrated it with a glass substrate photoacoustic transducer. In this chapter, we demonstrate the effect of photoacoustic shock waves such as jetting within a capillary tube, passage through a bubbly cloud, near a water-glass interface and reflection from a water-air interface. The results provide a foundation for later potential applications of photoacoustic from 3D printed substrates in microfluidics and cavitation related applications.

It may be good to focus a bit on the speed of the jet in droplet experiment. There you see a 100 m/s jet, while the jet from the convex interface is much slower. The droplet interface is

pretty flat (small contact angle) thus the jetting does not originate from the interface curvature. It may be due to the curvature of the focusing wave. You may want to elaborate that this curvature of the wave front may offer opportunities to create fast jets.

5.2 Experiment

In order to observe the interaction between the photoacoustic wave on the interface and with the bubbles, we conducted five experiments in this chapter. Similar to Chapter 3, the experiment setup was composed by two parts, one part for generation of photoacoustic waves and the other one for imaging. We kept the first part to generate the photoacoustic wave the same as Chapter 3, as shown in Figure 3.8. As for the imaging part, in this case, our purpose was to record the entire process of experiments, which required higher frame rate to observe the detailed process rather than a full size view of the shockwave. Therefore, we no longer utilized the shadowgraphy imaging method. Instead, we introduced the high speed camera system (Photron, SAX 1 and SAX 2, USA) to monitor and record the experiment. Correspondingly, the light source for illuminating was replaced by a powerful white LED light source (LS-M250/350, Sumita Optical Glass. Inc, Japan) instead of the pulse laser, without using any illuminating dye. The objective lenses were changed to 5X camera lens (Canon, working distance 65mm, magnification 5X), 5X long working distance objective lens and 20X long working distance objective lens (Mitutoyo, Japan) respectively. In the following experiment, all the time zero points refer to the moment when the laser light was output from the instrument.

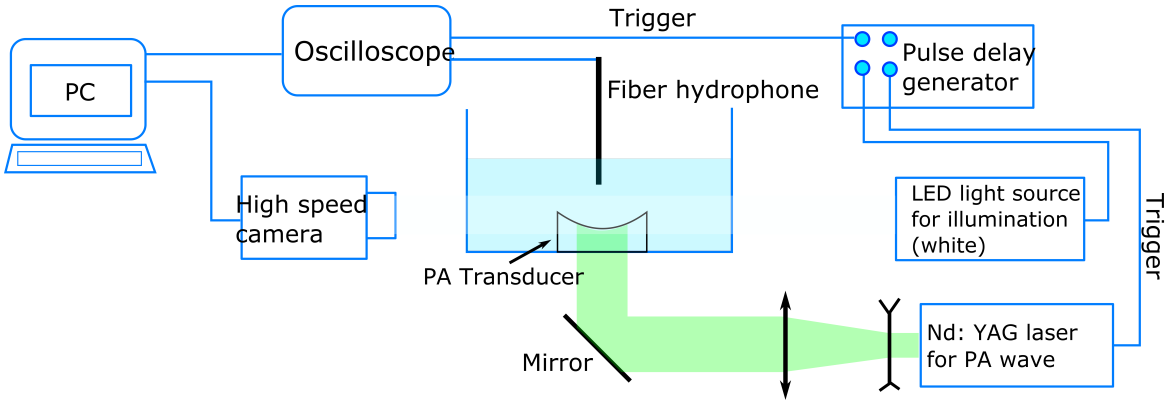

Fig. 5.1 Illustration of the experimental setup for poly-dispersed bubble – shockwave interaction.

5.3 Poly-dispersed bubble – shockwave interaction

Previous literatures reveal that the shock wave interacts with gas bubbles and causes strong changes to the bubbles [61]. In this section, we tried to demonstrate how the interaction happens when the photoacoustic shockwave passes through the bubble cloud. We need to generate bubble cloud inside water first. Thus, we used one additional 532 nm Nd:YAG laser (Oricon, NewWave, 6ns, maximum energy 8 mJ/pulse). The laser beam was focused into a $\sim$200 μm spot in water by using a 4X microscope objective lens (Olympus, Japan). The location of the beam spot was located within the focal area of the transducer, as shown in Figure 5.2. The photoacoustic transducer was placed perpendicularly to the direction of the focused laser beam by controlling the motorized stage.

A single large bubble was generated from instant heating of water by the focused laser, which was caused by the focused pulse laser. After the large laser-induced bubble (diameter $>$ 300 μm) collapsed, clouds of dispersed small bubbles (diameter $<$ 20 μm) appeared nearby within time delay of several microseconds as shown in Figure 5.3. At the moment,

the photoacoustic shockwave was synchronized to pass by this region. As shown in Figure 5.4(a), the cloud of small bubbles experienced a strong stretch in size and coalescences with surrounding bubbles afterwards. The change of the radius could be as large as four times of the original size. The entire expanding process happened in a short period of 6 μs and the succeeding oscillation of the bubbles lasted hundreds of microseconds. If the photoacoustic pressure was reduced to 150 bar by tuning the input laser power, we noticed that the stretching of the bubbles was apparently smaller than Figure 5.4(a). The duration of the bubble stretch was shorter than the case of 500 bar.

The typical frequency of the photoacoustic shockwave in this thesis was taken as 8 MHz. According to the estimation from Minnaert resonance [55], the resonance frequency of one bubble in water is

$$f \approx \frac{3.26}{r} \tag{5.1}$$

If the bubble size was 10 μm in diameter, the Minnaert frequency was nearly 0.8 MHz. While in this case, all the surrounding bubbles interacted together. The passing shockwave was scattered by bubbles.

5.4 Shockwave induced jet in the capillary tube

Research has been done on high speed jet induced by different approach [20, 63], such as laser and photoacoustic shockwaves. The speed of jet could hundreds of m/s if induced by a highly focused laser. In this section, we utilized the photoacoustic shockwave by the 3D printed transducer as the source to do the jet experiment.

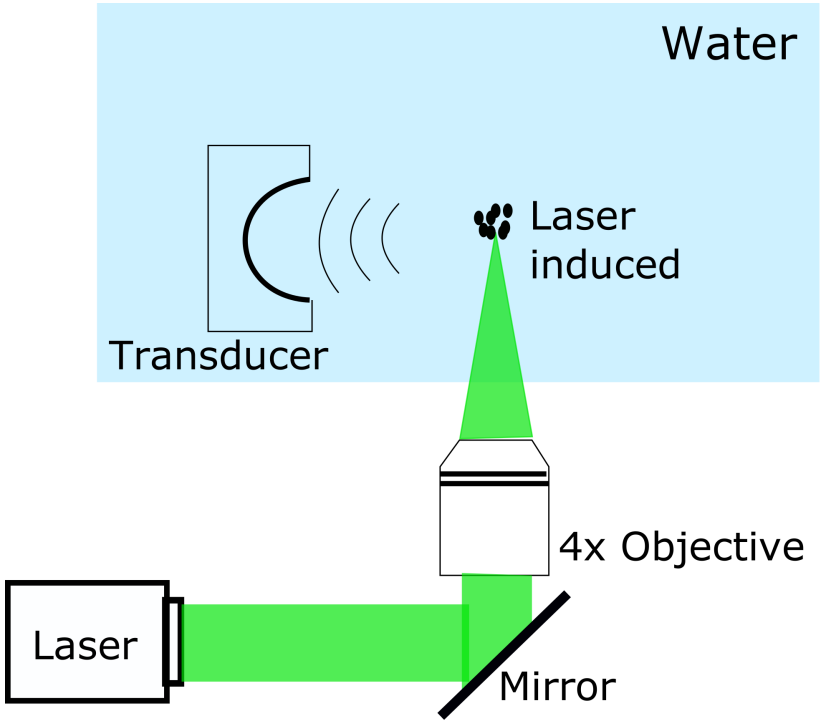

Fig. 5.2 Illustration of the experimental setup for poly-dispersed bubble – shockwave interaction

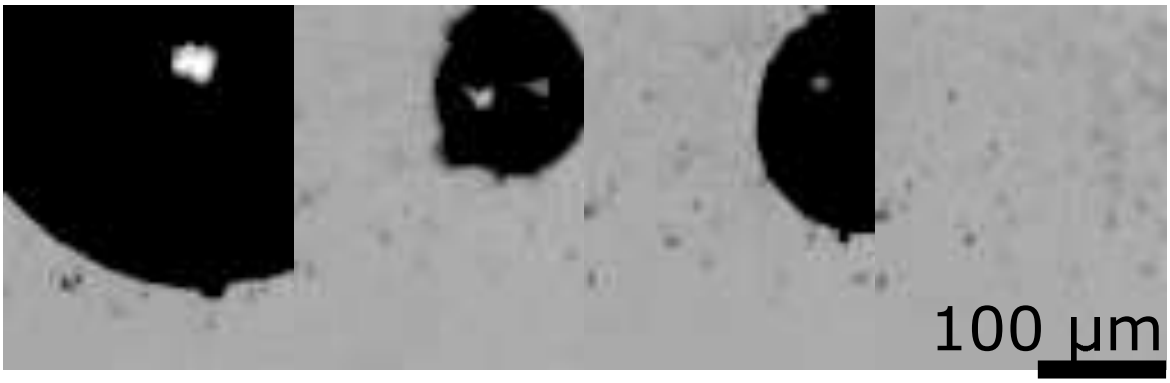

Fig. 5.3 Small bubble cloud following the collapes of the laser induced bubble

The 300 μm width glass capillary tube (fabricated in Nanyang Technological University, mechanical engineering lab) was hang at the focal area of the transducer. The internal diameter of the tube was 200 μm. The tip of the capillary tube was immersed inside water so

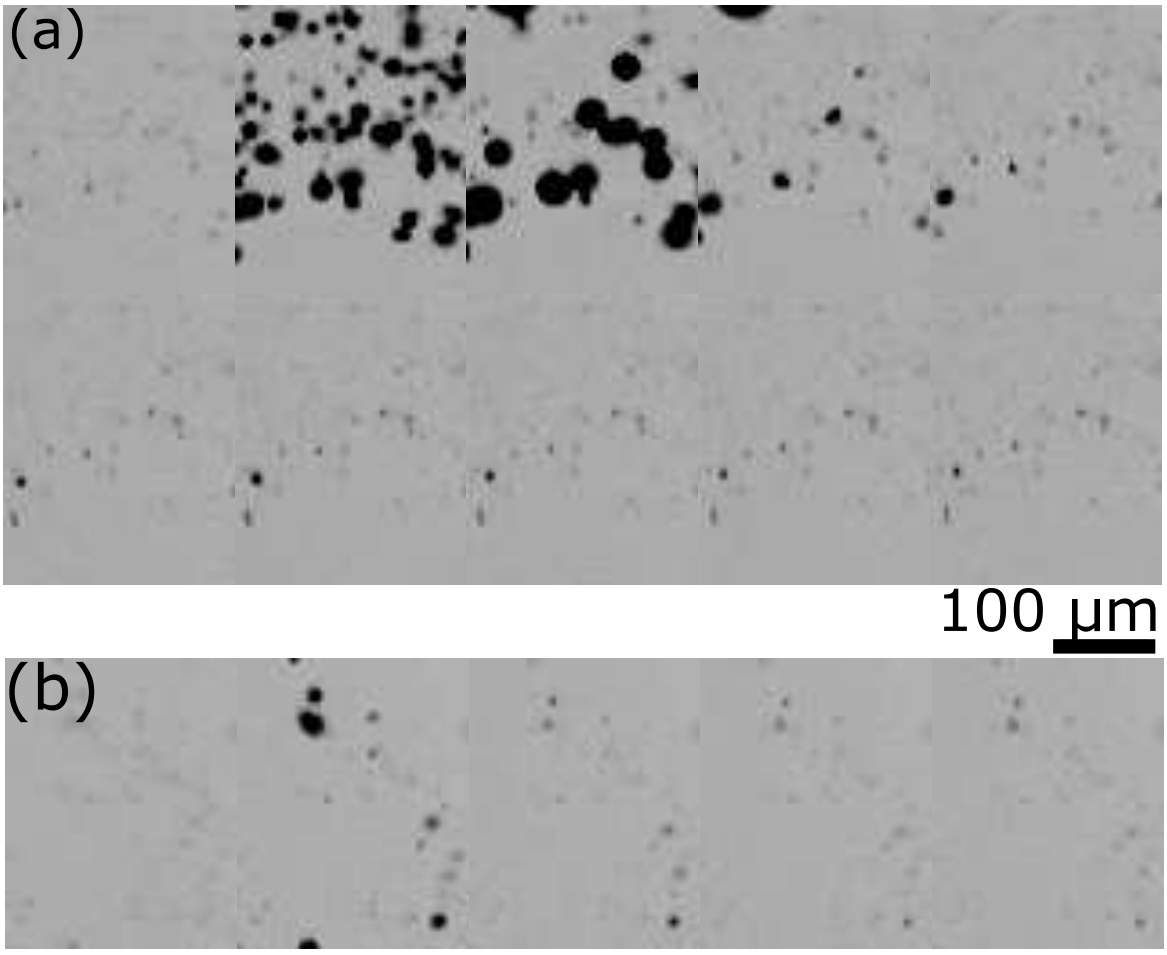

Fig. 5.4 Expansion of bubble cloud, time interval of each frame 3 μs. (a) Case of the improved transducer with maximum pressure $\sim$500 bar; (b) case of the original setting transducer with maximum pressure $\sim$150 bar.

that meniscus appeared 300 μm near the opening. The tip of the capillary tube was controlled by the 3D motorized stage to move within the focal area of the pressure.

In Figure 5.7, the strong cavitation was induced at the tip of the capillary tube at the first stage. As the cavitation started to collapse and moved away from the meniscus, the jet appeared at the surface of the meniscus inside the tube. The result verified the narrow spatial resolution of the acoustic pressure. We could observe the clear jet inside the capillary with the diameter around 80 μm. As shown in Figure 5.8, the height of the jet could reach 500

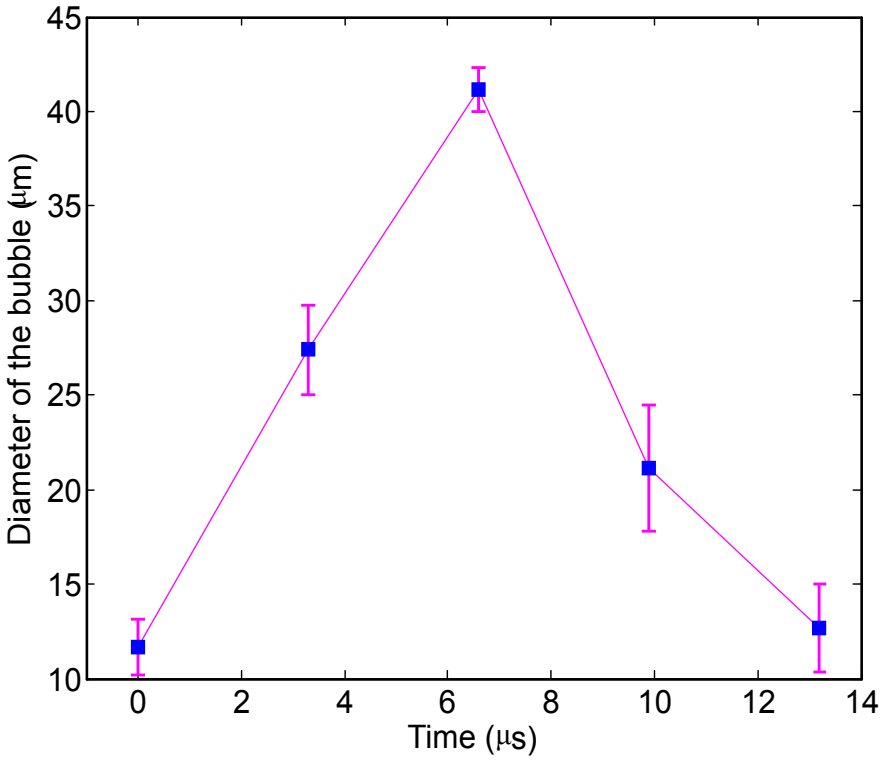

Fig. 5.5 Bubble diameter versus time (with the improved transducer). The error bar indicates the standard deviation of the diameter measurements.

μm with in 50 μs. However, in this case, the speed of the jet was not sufficiently fast, with the fasted speed of $\sim$30 m/s at the very first. Since the pressure wave from the transducer is highly localized, the slight misalignment caused splash of the jet. The shape of the jet was not straight, which resulted in slower speed of the jet.

5.5 Cavitation and jet at the water-air interface

The phase shift happens when the incident wave hits the interface of two different materials, so does the photoacoustic waves. The photoacoustic wave is changed in phase by 180°, when it is incident on the water-air interface. In order to explore the condition for the

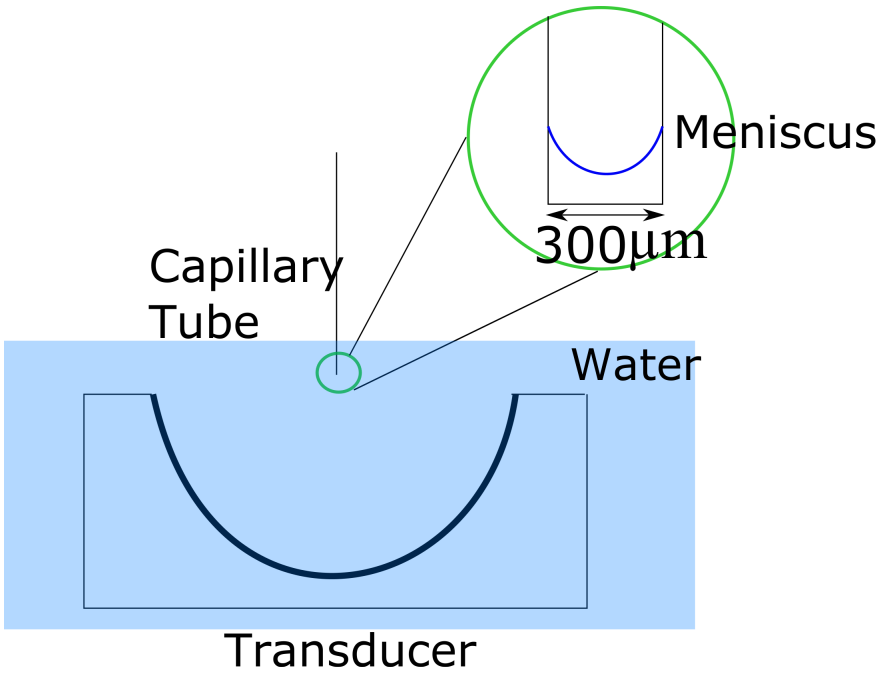

Fig. 5.6 Illustration of the experiment of jetting in the glass capillary tube.

photoacoustic wave to induce cavitation, we designed the following experiment to observe how the shockwave behaves at the water-air interface, as illustrated in Figure 5.5. First, the location of the maximum pressure was determined by the scanning method as mentioned in the previous chapter. Then we lowered the water level to make the focus on the interface. The entire process was recorded by the high speed camera.

We can observe a strong transient cavitation happening within 4 μs after the laser was fired, followed by oscillation of the bubbles until the cavitation dispersed into small bubbles. Figure 5.10(a) shows the cavitation at the interface at the full input of laser. We noted that there was a threshold to induce the cavitation at the water-air interface, where the laser input was 8 mJ/pulse, as in Figure 5.10(b). The largest cavitation only lasted for less than 8 μs in this case, which was captured by one frame. When we further increased the laser input,

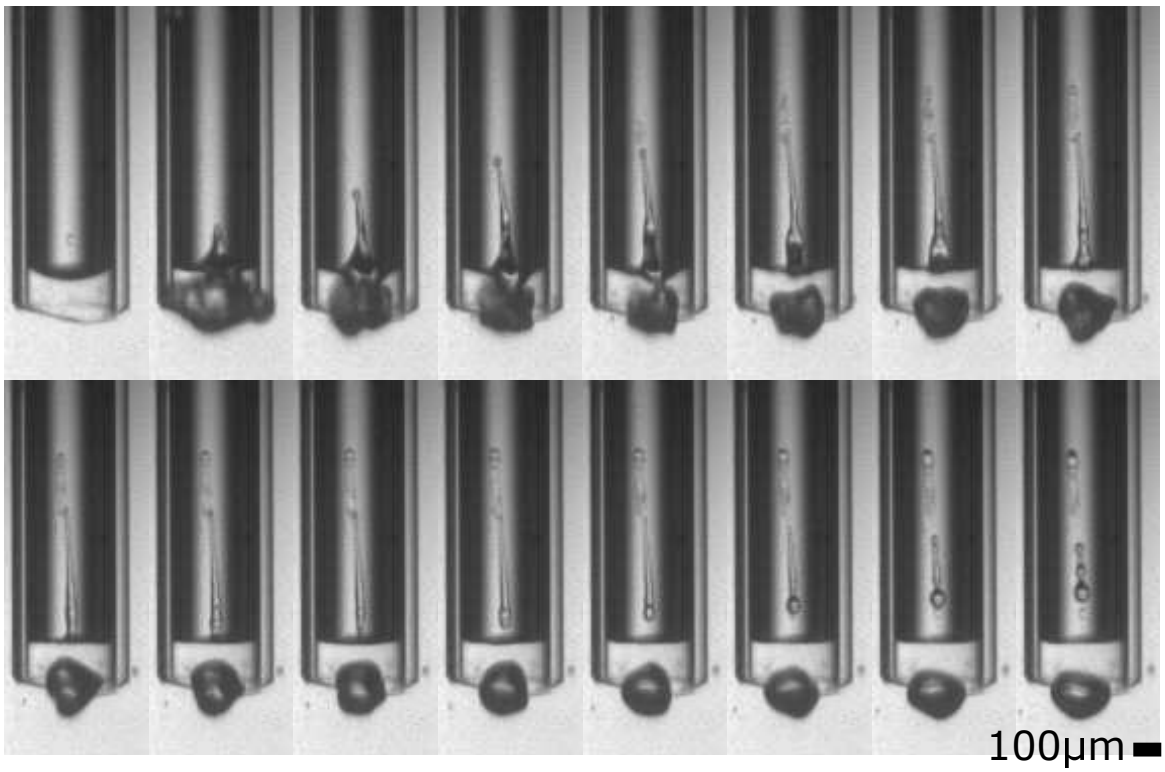

Fig. 5.7 Jetting inside the glass capillary tube with time interval of 4 μs.

the cavitation could exist for more than 20 μs before it reduced to poly-dispersed bubbles. The maximum size and lifetime of the cavitation was also revealed in the experiment. The size of the cavitation is dependent on the incident laser energy. Different laser input energy settings were applied as in Figure 5.11, where the cavitation size was 0 at the starting point. The maximum size and lifetime of the cavitation increased as the input energy was increased. The maximum size of the cavitation was around 300 μm. As the input laser energy was increase, the maximum size and lifetime of the cavitation also reduced from maximum 25 μs to less than 8 μs.

Figure 5.12 shows the jet which was induced by the photoacoustic pressure wave. The brightness of first frame is higher due to the incident strong green laser. First of the stage, the

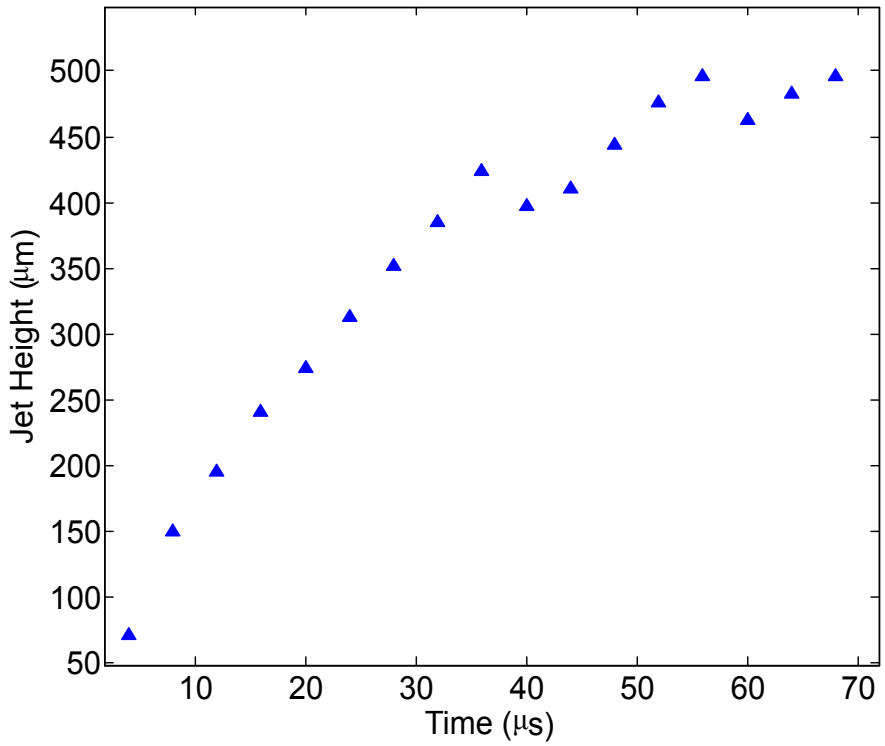

Fig. 5.8 Height of the jet before it hit the inner wall of the tube, corresponding to Figure 5.7

slashed jet happened at the interface, with fastest speed of 30 m/s. After splashing, a droplet in diameter of 300 μm was generated, moved upward and dropped back to the surface after 40 ms, which was much slower than the initial jet.

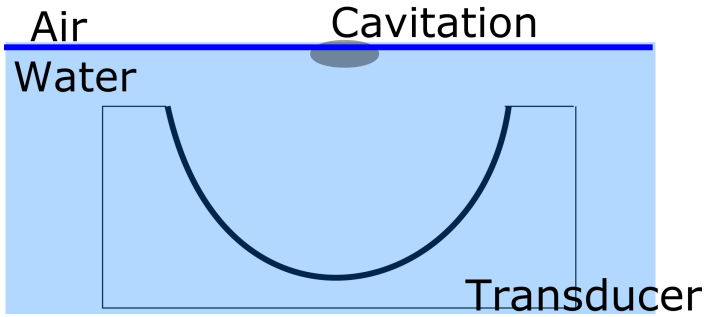

Fig. 5.9 Illustration of the experiment of the interfacial cavitation.

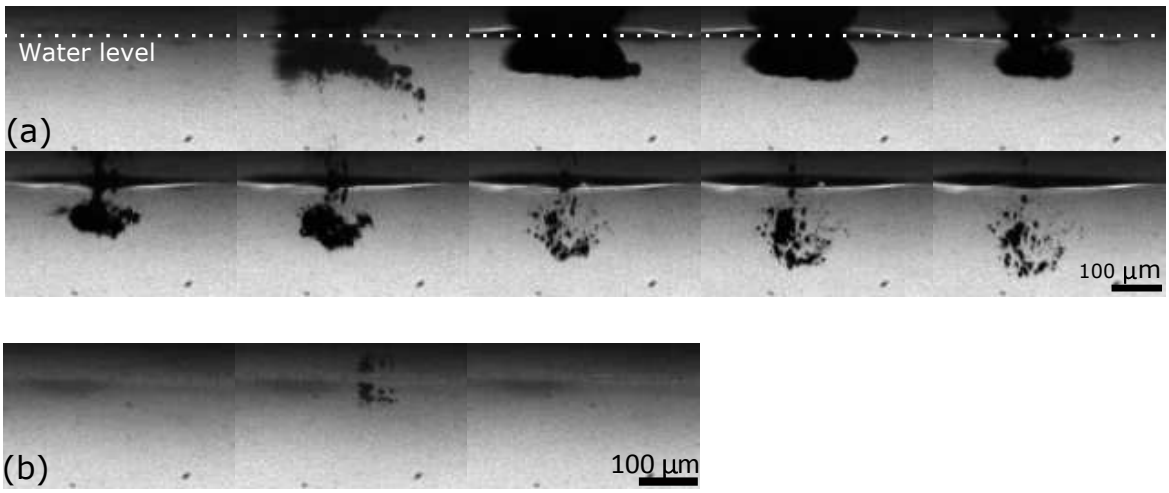

Fig. 5.10 Cavitation at the water – air interface. The time interval between frames is 4 μs: (a) at full energy input 16 mJ/pulse; (b) at 8 mJ/pulse.

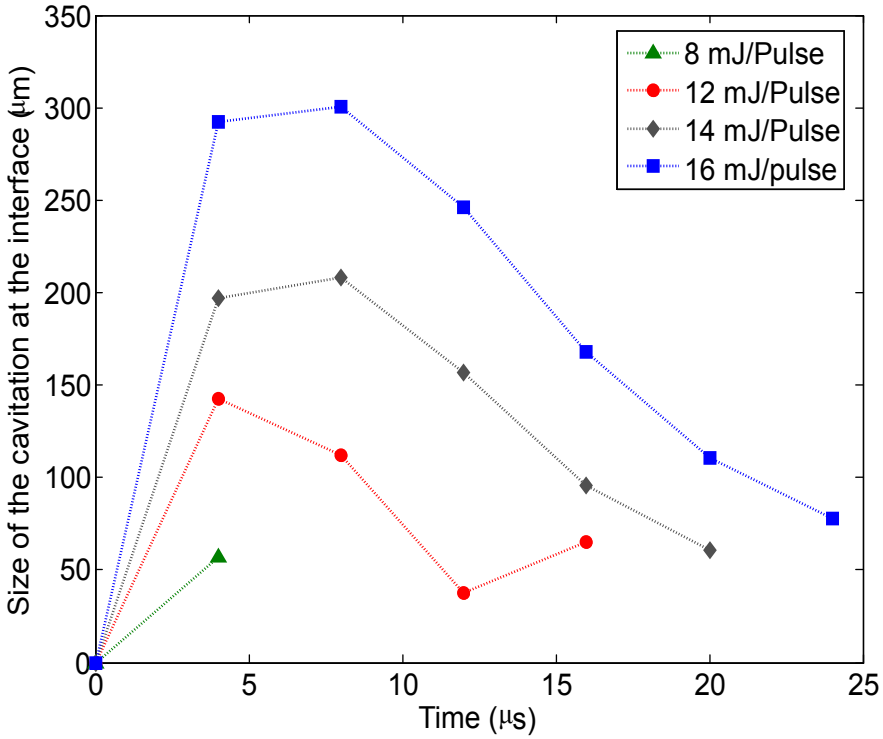

Fig. 5.11 Cavitation size versus time at different settings of input laser energy

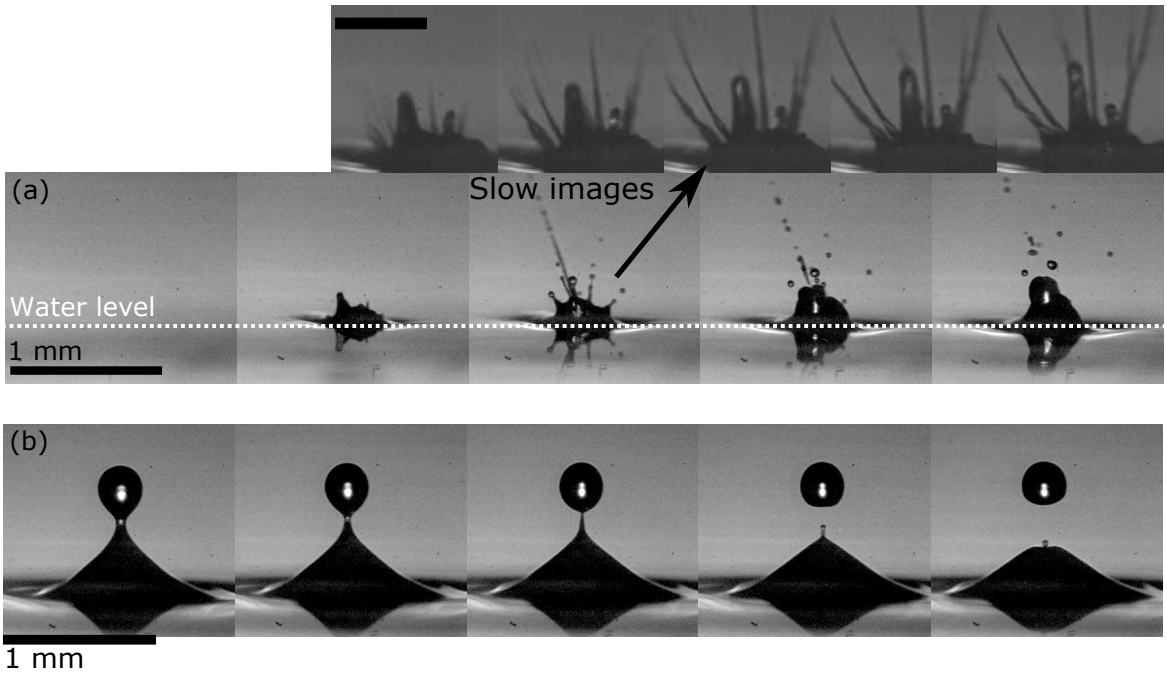

Fig. 5.12 Jet at the water – air interface with time interval of 40 μs. (a) Splashed jet at the interface (with slow images with time interval of 5.5 μs); (b) Drop generated from the interface.

5.6 Cavitation at the water-glass interface

We tried to find the effect of the photoacoustic wave when it hit the hard surface. The hard surface will lead to the phase change of the incident wave. The positive and negative pressure peaks experienced 180° phase change. We expected that the reflective wave would cause cavitation at the interface. In this experiment, we used the glass fiber from the hydrophone with the diameter of 125 μm and placed exactly at the focal point, where the maximum pressure value was detected. After finding the maximum pressure, the hydrophone laser was turned off to avoid over exposure to the sensor of the camera, and the cavitation at the tip was observed by the sCOMS camera system.

From the calculation in Chapter 3 shown in Figure 4.9, we know that the mechanism of the cavitation in this case is induced by the reflective pressure and the diffraction pressure wave from the corner of the fiber. Figure 5.15 shows the process from the appearance of the cavitation to the collapse. When the pressure wave hit the tip, a reflective wave was produced. The cavitation happened after ~0.5 μs after the positive pressure wave passed by. The cavitation oscillated at the tip of the fiber until it collapsed. The maximum size could reach 30 μm in diameter.

When the cavitation happened at the tip, the fiber optical hydrophone detected strong negative pressure value, as shown in Figure 5.14. The negative pressure value can be near 300 bar, which is tens of times stronger than the positive pressure. From the reading, the bubble could last a short time of 5 μs followed by a size bounce of 1.5 μs.

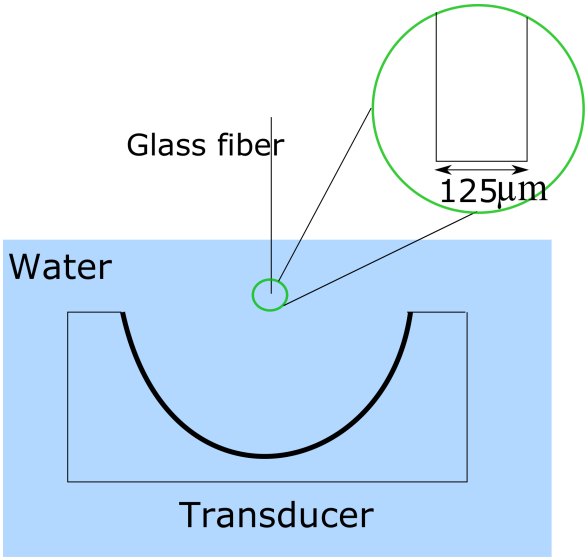

Fig. 5.13 Illustration of the experiment of the water-glass interfacial cavitation.

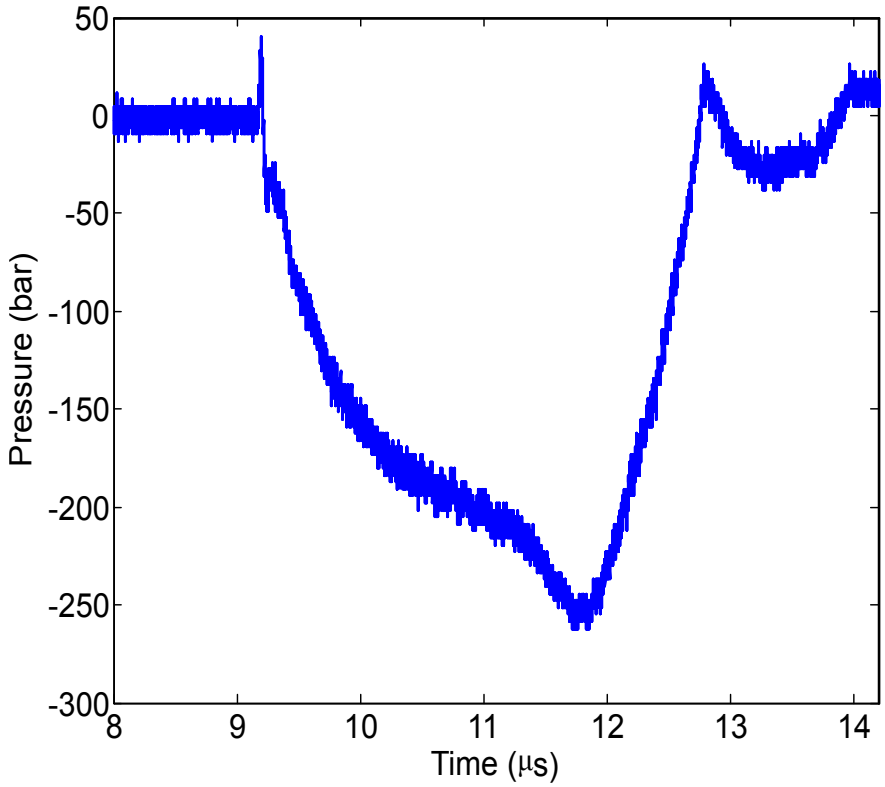

Fig. 5.14 Hydrophone reading of cavitation on the water–glass interface

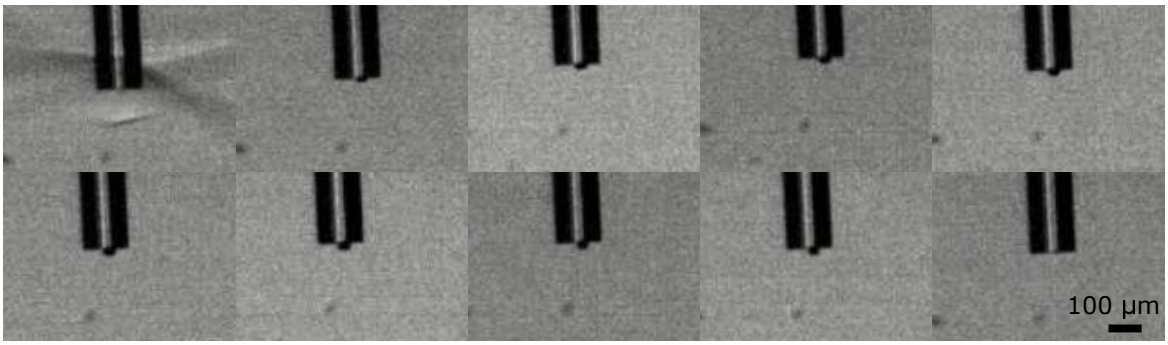

Fig. 5.15 Cavitation on the water–glass interface, time interval of two frames 0.5 μs

5.7 Cavitation and jet in the small droplet

We designed a setup to visualize the cavitation and jet along the droplet surface. The top of the transducer was covered and fixed tightly with a thin Teflon film (Dupont, USA, stretched to 80 – 100 μm in thickness), as in Figure 5.16. With the small syringe needle (0.8 mm diameter), deionized water was injected into the chamber. We still applied the same scanning method to find the maximum pressure on the Teflon film. Later, the water level in the tank was lowered below the film. 100 μl deionized water was dropped at the focal area of the transducer. The thickness of the droplet was around 300 μm and the width was around 2.0 mm. From Figure 5.16 and 5.17, the photoacoustic wave induced two jets. The first jet had a higher maximum height around 800 μm and much faster speed around 100 m/s within 70 μs. While, the second jet had a maximum peak of 600 μm and slower speed of 2 m/s as in Figure 5.18. The second jet could last more than 100 μs.

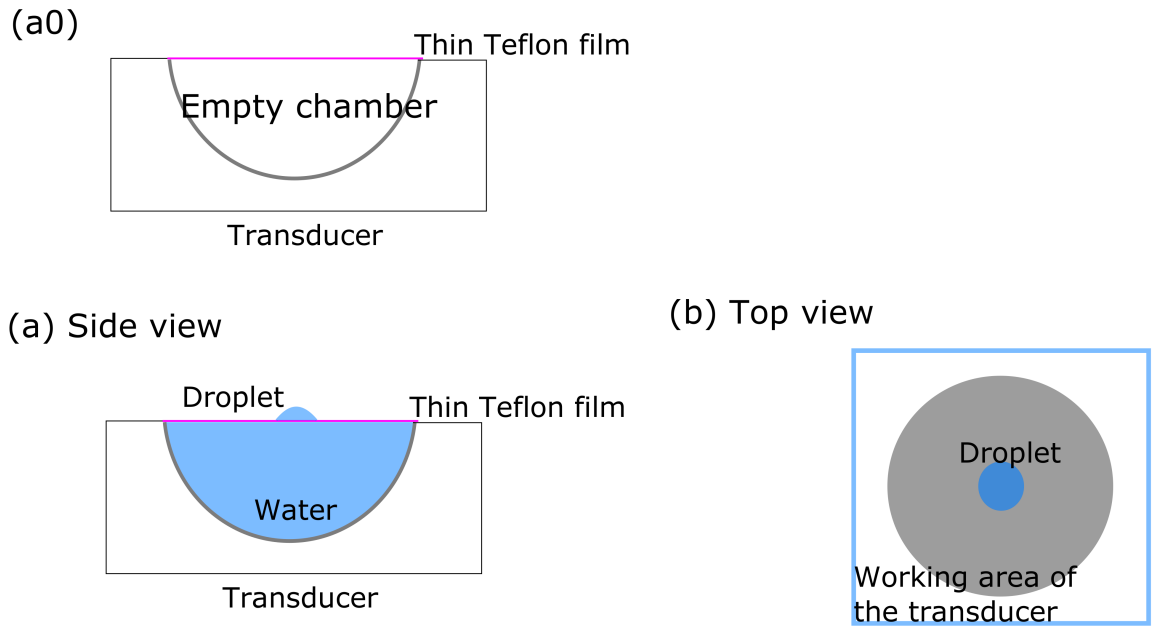

Fig. 5.16 Illustration of the experiment for shockwave inside the droplet

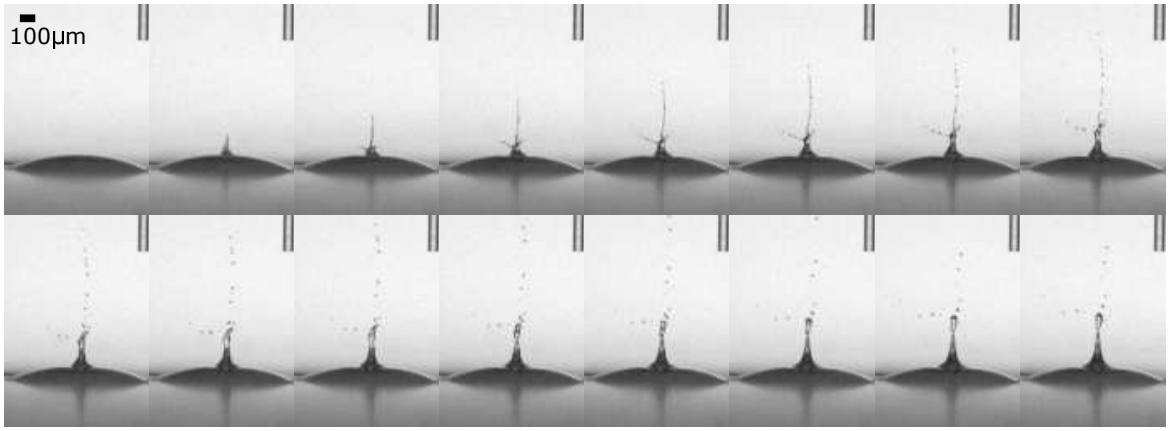

Fig. 5.17 The jet from the surface of a small drop with time interval of 10 μs

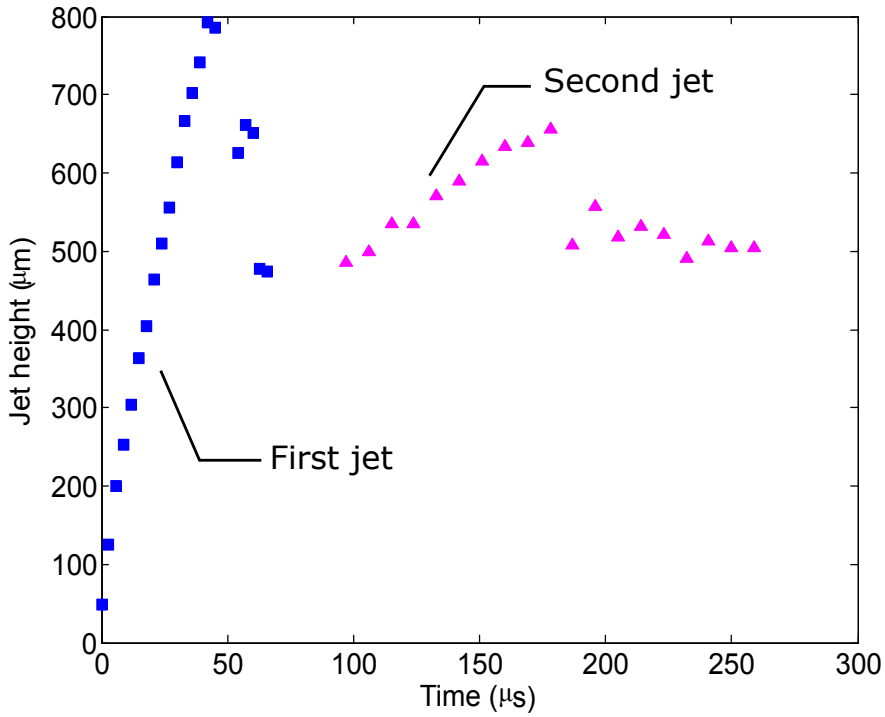

Fig. 5.18 Jet height versus time, from the same experimental record of Figure 5.17, with time interval $\sim$3 μs.

Due to the restriction of illumination, we increased the volume of the droplet so that we could have a view through the droplet. If we increased the thickness of the droplet to around 1 mm, we might see more clearly what happened inside. From the images captured by the

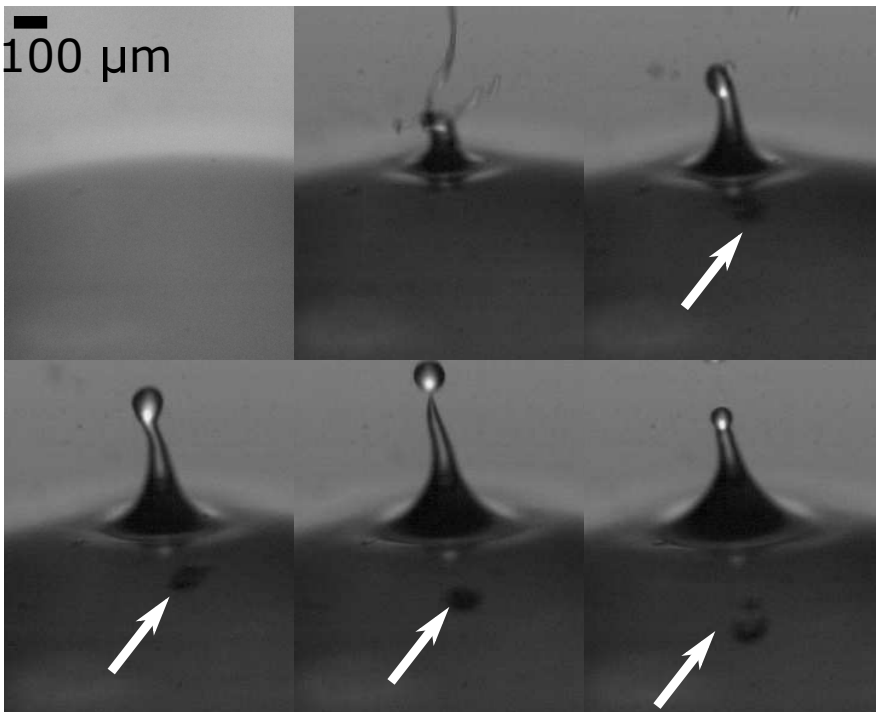

Fig. 5.19 Cavitation inside the droplet (white arrows show the cavitation inside the drop). Time interval 50 μs.

high speed camera in Figure 5.19, we could observe that near the inner surface of the droplet, cavitation was induced by the acoustic pressure. The size of the cavitation was around 100 μm. When the bubble moved downwards, the jet appeared at the surface of the droplet. The situation was similar with section 5.5, while the first jet speed was faster.

Chapter 6

Conclusion and outlook

6.1 Conclusion

In this thesis, the novel method has been developed to fabricate the photoacoustic transducer based on 3D printing technology and room temperature physical deposition. 3D printing technology has played an important function in manipulating the geometry and fabricating the photoacoustic transducer. Through this approach, the substrate of the photoacoustic transducer can be flexibly customized by 3D graphics data, without involving any carving, machining or high temperature process. We managed to make out the spherical transducer, two-stepped transducer, cross-stepped transducer and provided the possibility of more other shaped transducers. The spherical transducer was proven to generate the high acoustic pressure of 500 bar with the spatial precision of 500 μm, which is highly localized and sufficiently high through the pressure distribution mapping. As expected, the corresponding wavefronts were consistent with the geometries of the transducer. We were able to obtain two separated wavefronts with desirable time difference and peak values. The results were

supported by calculation. The results confirm the feasibility of the photoacoustic transducer by 3D printing to work towards realization to control the spatial and temporal distribution of ultrasonic energy.

Some auxiliary methods are also developed as alternatives to fabricate the transducer, including PDMS casting and droplet-method. By applying these methods, it is possible to fabricate small size transducers within shorter time, less cost and less handling procedures. The transducer can highly maintain the precision spatial resolution of pressure under some compromise to the amplitude. The transducer fabricated by theses methods could generate pressure up to ∼60 bar. The droplet transducer could reach ∼50 bar within 500 μm precision at the surface of glass. This result is believed to be useful in the future work related with microfluidics and acoustic experiments on hard surfaces. Table 6.1 shows a summary for the pressure obtained so far.

Table 6.1 Summary of the pressures of different types of transducers

Type	Max positive pressure(bar)	Shape
Glass-based	∼120	Spherical
Veroclear	∼80	Spherical
Resin	>500	Spherical
PDMS casting	∼60	Spherical
Droplet type	∼40	Focused (formed by gravity)

The 3D printed transducer can be used to induce cavitation and jet in different interfaces. With the positive pressure of 500 bars induced by the transducer, the cavitation can be

generated at the water-air interface. In the same experimental conditions, the jet also happened at the interface of water-glass and curved interfaces, like bubble surface and meniscus. The faster jet speed could be achieved if we utilized the shockwave to droplet. The curvature of the droplet enhanced the jet speed to about 100 m/s. In the capillary tube, with the help of meniscus, the jet speed was $\sim$30 m/s. Additionally, on the water-glass interface, the strong acoustic pressure could induce the cavitation onward with the size of tens of micrometers. The negative pressure of the cavitation could be tens of times of the positive pressure. Conclusively, the transducer can be considered as an alternative of the piezoelectric or glass transducers in the future research and applications.

6.2 Outlook and future work

We have the vision of the future work of three directions. Integrated devices of small scale can be considered to fabricate. For example, 3D printing technology provides the feasibility of integrating the photoacoustic transducer into microfluidic devices. Previous literature has shown a lot of research in the devices, which are combined of microchannels and transducer. One research has shown a potentially efficient way to delivery drugs [80]. It is also reported that 3D printed microchannels have been proven applicable in chemical reaction, cellular analysis or biomedical research [81, 82]. Inspired by these prior results, we consider combing the two components so that it is possible to provide a one-stop approach for further study in microfluidics. We are trying to make the photoacoustic shockwave focus inside the microlevel channel ($300\mu m \sim 500\mu m$, which is the range of good printing quality below centimeter

level). We expect that this kind of device can be utilized to conduct the experiment of particle-shockwave interaction, microbubble-shockwave interaction or further cell stretch or deformation.

The improvement can be continuously made to further increase the energy converting efficiency, precision of the pressure wave and pressure amplitude, especially the negative pressure. Free field cavitation is still the concern in our case. Although the positive pressure has already reached 500 bar, the negative pressure did not increase largely. This led to the failure in inducing free field cavitation in water. The possible solution may be exploring more materials and refining the fabrication to make even stronger and faster thermal relaxation of the light-absorbing film. Once the free-field cavitation can be realized, the device can be used to in the preliminary experiments for developing applications, such as tissue removal, lithotripsy or imaging.

Furthermore, various complicated geometries of the photoacoustic transducers can be explored. In this thesis, we focused on demonstration of the spherical based transducer and generation of high pressure. In fact, more sophisticated designs can be achieved. The acoustic devices can be diversified through this technology. Large size acoustic devices are also available. We are making efforts on fabricating like acoustic Fresnel transducer, multi-focus transducer, and surface tunable transducer. In our outlook, it is feasible to realize full customization of acoustic devices.

Bibliography

[1] Weiwei Chan, Thomas Hies, and Claus-Dieter Ohl. Laser-generated focused ultrasound for arbitrary waveforms. *Applied Physics Letters*, 109(17):174102, 2016.

[2] Yang Hou, Jin-Sung Kim, Shai Ashkenazi, Sheng-Wen Huang, L Jay Guo, and Matthew O'Donnell. Broadband all-optical ultrasound transducers. *Applied Physics Letters*, 91(7):073507, 2007.

[3] Hyoung Won Baac, Jong G Ok, Adam Maxwell, Kyu-Tae Lee, Yu-Chih Chen, A John Hart, Zhen Xu, Euisik Yoon, and L Jay Guo. Carbon-nanotube optoacoustic lens for focused ultrasound generation and high-precision targeted therapy. *Sci. Rep.*, 2, 2012.

[4] Wei-Yi Chang, Wenbin Huang, Jinwook Kim, Sibo Li, and Xiaoning Jiang. Candle soot nanoparticles-polydimethylsiloxane composites for laser ultrasound transducers. *Appl. Phys. Lett*, 107(16):161903, 2015.

[5] Jean-Pierre Kruth, Peter Mercelis, J Van Vaerenbergh, Ludo Froyen, and Marleen Rombouts. Binding mechanisms in selective laser sintering and selective laser melting. *Rapid prototyping journal*, 11(1):26–36, 2005.

[6] Acoustical Terminology. American national standard. *ANSI S1*, pages 1–1994.

[7] Hyoung Won Baac, Taehwa Lee, Jong G Ok, Timothy Hall, and L Jay Guo. Dual-frequency focused ultrasound using optoacoustic and piezoelectric transmitters for single-pulsed free-field cavitation in water. *Appl. Phys Lett.*, 103(23):234103, 2013.

[8] James E Kennedy. High-intensity focused ultrasound in the treatment of solid tumours. *Nature reviews cancer*, 5(4):321–327, 2005.

[9] PS Sidhu. Clinical and imaging features of testicular torsion: Role of ultrasound: Review. *Clinical radiology*, 54(6):343–352, 1999.

[10] Shahram Vaezy, Xuegong Shi, Roy W Martin, Emil Chi, Peter I Nelson, Michael R Bailey, and Lawrence A Crum. Real-time visualization of high-intensity focused ultrasound treatment using ultrasound imaging. *Ultrasound in medicine & biology*, 27(1):33–42, 2001.

[11] Takashi Buma, Monica Spisar, and Matthew O'Donnell. Thermoelastic expansion vs. piezoelectricity for high-frequency, 2-d arrays. *ieee transactions on ultrasonics, ferroelectrics, and frequency control*, 50(8):1065–1068, 2003.

[12] SJ Davies, Chris Edwards, GS Taylor, and Stuart B Palmer. Laser-generated ultrasound: its properties, mechanisms and multifarious applications. *Journal of Physics D: Applied Physics*, 26(3):329, 1993.

[13] S. Boonsang. Photoacoustic generation mechanisms and measurement systems for biomedical applications, 2009.

[14] Nan Wu, Ye Tian, Xiaotian Zou, Vinicius Silva, Armand Chery, and Xingwei Wang. High-efficiency optical ultrasound generation using one-pot synthesized polydimethylsiloxane-gold nanoparticle nanocomposite. *JOSA B*, 29(8):2016–2020, 2012.

[15] Hyoung Won Baac, Jong G Ok, Taehwa Lee, and L Jay Guo. Nano-structural characteristics of carbon nanotube–polymer composite films for high-amplitude optoacoustic generation. *Nanoscale*, 7(34):14460–14468, 2015.

[16] Bao-Yu Hsieh, Jinwook Kim, Jiadeng Zhu, Sibo Li, Xiangwu Zhang, and Xiaoning Jiang. A laser ultrasound transducer using carbon nanofibers–polydimethylsiloxane composite thin film. *Appl. Phys. Lett*, 106(2):021902, 2015.

[17] L. M. Lyamshev and K. A. Naugolnykh. Optical generation of sound-nonlinear effects. *Soviet Physics Acoustics-Ussr*, 27(5):357–371, 1981.

[18] Lihong V Wang and Hsin-i Wu. *Biomedical optics: principles and imaging*. John Wiley & Sons, 2012.

[19] LH Tong, CW Lim, and YC Li. Generation of high-intensity focused ultrasound by carbon nanotube opto-acoustic lens. *J. Appl. Mech.*, 81(8):081014, 2014.

[20] Hyoung Won Baac, Taehwa Lee, and L Jay Guo. Micro-ultrasonic cleaving of cell clusters by laser-generated focused ultrasound and its mechanisms. *Biomed. Opt. Express*, 4(8):1442–1450, 2013.

[21] Richard J Colchester, Charles A Mosse, Davinder S Bhachu, Joseph C Bear, Claire J Carmalt, Ivan P Parkin, Bradley E Treeby, Ioannis Papakonstantinou, and Adrien E Desjardins. Laser-generated ultrasound with optical fibres using functionalised carbon nanotube composite coatings. *Appl. Phys. Lett*, 104(17):173502, 2014.

[22] Richard M White. Generation of elastic waves by transient surface heating. *Journal of Applied Physics*, 34(12):3559–3567, 1963.

[23] Yang Hou, Shai Ashkenazi, Sheng-wen Huang, and Matthew O'Donnell. Improvements in optical generation of high-frequency ultrasound. *IEEE transactions on ultrasonics, ferroelectrics, and frequency control*, 54(3), 2007.

[24] AL McKenzie. Physics of thermal processes in laser-tissue interaction. *Physics in medicine and biology*, 35(9):1175, 1990.

[25] H Raether. Surface plasma oscillations as a tool for surface examinations. *Surface Science*, 8(1-2):233–246, 1967.

[26] Xin Liu and Mark T Swihart. Heavily-doped colloidal semiconductor and metal oxide nanocrystals: an emerging new class of plasmonic nanomaterials. *Chemical Society Reviews*, 43(11):3908–3920, 2014.

[27] Yang Hou, Jin-Sung Kim, Shai Ashkenazi, Matthew O'Donnell, and L Jay Guo. Optical generation of high frequency ultrasound using two-dimensional gold nanostructure. *Applied physics letters*, 89(9):093901, 2006.

[28] LW Kessler, A Korpel, and PR Palermo. Simultaneous acoustic and optical microscopy of biological specimens. *Nature*, 239(5367):111–112, 1972.

[29] Richard SC Cobbold. *Foundations of biomedical ultrasound*. Oxford University Press, 2006.

[30] GJ Diebold, T Sun, and MI Khan. Photoacoustic monopole radiation in one, two, and three dimensions. *Physical review letters*, 67(24):3384, 1991.

[31] GJ Diebold and T Sun. Properties of photoacoustic waves in one, two, and three dimensions. *Acta Acustica united with Acustica*, 80(4):339–351, 1994.

[32] Elena Biagi, Fabrizio Margheri, and David Menichelli. Efficient laser-ultrasound generation by using heavily absorbing films as targets. *ieee transactions on ultrasonics, ferroelectrics, and frequency control*, 48(6):1669–1680, 2001.

[33] Minghua Xu and Lihong V Wang. Photoacoustic imaging in biomedicine. *Review of scientific instruments*, 77(4):041101, 2006.

[34] Seok Hwan Lee, Mi-ae Park, Jack J Yoh, Hyelynn Song, Eui Yun Jang, Yong Hyup Kim, Sungchan Kang, and Yong Seop Yoon. Reduced graphene oxide coated thin aluminum film as an optoacoustic transmitter for high pressure and high frequency ultrasound generation. *Applied Physics Letters*, 101(24):241909, 2012.

[35] Q Zhang, N Iwakuma, P Sharma, BM Moudgil, C Wu, J McNeill, H Jiang, and SR Grobmyer. Gold nanoparticles as a contrast agent for in vivo tumor imaging with photoacoustic tomography. *Nanotechnology*, 20(39):395102, 2009.

[36] Wei Lu, Qian Huang, Geng Ku, Xiaoxia Wen, Min Zhou, Dmitry Guzatov, Peter Brecht, Richard Su, Alexander Oraevsky, Lihong V Wang, et al. Photoacoustic imaging of living

mouse brain vasculature using hollow gold nanospheres. *Biomaterials*, 31(9):2617–2626, 2010.

[37] Xueding Wang, Yongjiang Pang, Geng Ku, Xueyi Xie, George Stoica, and Lihong V Wang. Noninvasive laser-induced photoacoustic tomography for structural and functional in vivo imaging of the brain. *Nature biotechnology*, 21(7):803–806, 2003.

[38] Srivalleesha Mallidi, Geoffrey P Luke, and Stanislav Emelianov. Photoacoustic imaging in cancer detection, diagnosis, and treatment guidance. *Trends in biotechnology*, 29(5):213–221, 2011.

[39] Taehwa Lee, Jong G Ok, L Jay Guo, and Hyoung Won Baac. Low f-number photoacoustic lens for tight ultrasonic focusing and free-field micro-cavitation in water. *Appl. Phys. Lett.*, 108(10):104102, 2016.

[40] Taehwa Lee, Hyoung Won Baac, Jong G Ok, Hong Seok Youn, and L Jay Guo. Nozzle-free liquid microjetting via homogeneous bubble nucleation. *Physical Review Applied*, 3(4):044007, 2015.

[41] Kaufui V Wong and Aldo Hernandez. A review of additive manufacturing. *ISRN Mechanical Engineering*, 2012, 2012.

[42] Chee Kai Chua, Kah Fai Leong, and Chu Sing Lim. *Rapid prototyping: principles and applications*. World Scientific, 2010.

[43] Fabian Rengier, A Mehndiratta, Hendrik von Tengg-Kobligk, Christian M Zechmann, Roland Unterhinninghofen, H-U Kauczor, and Frederik L Giesel. 3d printing based on imaging data: review of medical applications. *International journal of computer assisted radiology and surgery*, 5(4):335–341, 2010.

[44] Carl Schubert, Mark C Van Langeveld, and Larry A Donoso. Innovations in 3d printing: a 3d overview from optics to organs. *British Journal of Ophthalmology*, 98(2):159–161, 2014.

[45] Hideo Kodama. Automatic method for fabricating a three-dimensional plastic model with photo-hardening polymer. *Review of scientific instruments*, 52(11):1770–1773, 1981.

[46] Ferry PW Melchels, Jan Feijen, and Dirk W Grijpma. A review on stereolithography and its applications in biomedical engineering. *Biomaterials*, 31(24):6121–6130, 2010.

[47] Alain Le Mehaute. The info list-stereolithography.

[48] Xue Yan and PENG Gu. A review of rapid prototyping technologies and systems. *Computer-Aided Design*, 28(4):307–318, 1996.

[49] W Lauterborn, Th Kurz, R Mettin, and CD Ohl. Experimental and theoretical bubble dynamics. *Advances in chemical physics*, 110:295–380, 1999.

[50] Ernest A Neppiras. Acoustic cavitation. *Physics reports*, 61(3):159–251, 1980.

[51] Alfred Vogel and Vasan Venugopalan. Mechanisms of pulsed laser ablation of biological tissues. *Chemical reviews*, 103(2):577–644, 2003.

[52] I Akhatov, O Lindau, A Topolnikov, R Mettin, N Vakhitova, and W Lauterborn. Collapse and rebound of a laser-induced cavitation bubble. *Physics of Fluids*, 13(10):2805–2819, 2001.

[53] W Lauterborn and H Bolle. Experimental investigations of cavitation-bubble collapse in the neighbourhood of a solid boundary. *Journal of Fluid Mechanics*, 72(2):391–399, 1975.

[54] Werner Lauterborn and Thomas Kurz. Physics of bubble oscillations. *Reports on progress in physics*, 73(10):106501, 2010.

[55] Christopher E Brennen. *Cavitation and bubble dynamics*. Cambridge University Press, 2013.

[56] Siew-Wan Ohl, Evert Klaseboer, and Boo Cheong Khoo. Bubbles with shock waves and ultrasound: a review. *Interface focus*, 5(5):20150019, 2015.

[57] Joseph B Keller and Michael Miksis. Bubble oscillations of large amplitude. *The Journal of the Acoustical Society of America*, 68(2):628–633, 1980.

[58] Forrest R Gilmore. The growth or collapse of a spherical bubble in a viscous compressible liquid. 1952.

[59] Robert T Beyer. Nonlinear acoustics. Technical report, BROWN UNIV PROVIDENCE RI DEPT OF PHYSICS, 1974.

[60] Yunus A Cengel, JOHN M Cimbala, et al. *Fundamental and applications*. McGraw Hill, New York, 2006.

[61] Devesh Ranjan, Jason Oakley, and Riccardo Bonazza. Shock-bubble interactions. *Annual Review of Fluid Mechanics*, 43:117–140, 2011.

[62] George Keith Batchelor. *An introduction to fluid dynamics*. Cambridge university press, 2000.

[63] Yoshiyuki Tagawa, Nikolai Oudalov, Claas Willem Visser, Ivo R Peters, Devaraj van der Meer, Chao Sun, Andrea Prosperetti, and Detlef Lohse. Highly focused supersonic microjets. *Physical review X*, 2(3):031002, 2012.

[64] Claas Willem Visser, Yoshiyuki Tagawa, Chao Sun, and Detlef Lohse. Microdroplet impact at very high velocity. *Soft matter*, 8(41):10732–10737, 2012.

[65] Yoshiyuki Tagawa, Nikolai Oudalov, A El Ghalbzouri, Chao Sun, and Detlef Lohse. Needle-free injection into skin and soft matter with highly focused microjets. *Lab on a Chip*, 13(7):1357–1363, 2013.

[66] CL Goodridge, HGE Hentschel, and DP Lathrop. Breaking faraday waves: critical slowing of droplet ejection rates. *Physical review letters*, 82(15):3062, 1999.

[67] Benjamin W Zeff, Benjamin Kleber, Jay Fineberg, and Daniel P Lathrop. Singularity dynamics in curvature collapse and jet eruption on a fluid surface. *Nature*, 403(6768):401–404, 2000.

[68] Michael S Longuet-Higgins. Vertical jets from standing waves. In *Proceedings of the Royal Society of London A: Mathematical, Physical and Engineering Sciences*, volume 457, pages 495–510. The Royal Society, 2001.

[69] I Apitz and A Vogel. Material ejection in nanosecond er: Yag laser ablation of water, liver, and skin. *Applied Physics A: Materials Science & Processing*, 81(2):329–338, 2005.

[70] D Obreschkow, Ph Kobel, N Dorsaz, A De Bosset, C Nicollier, and M Farhat. Cavitation bubble dynamics inside liquid drops in microgravity. *Physical review letters*, 97(9):094502, 2006.

[71] Etienne Robert, Jacques Lettry, Mohamed Farhat, Peter A Monkewitz, and François Avellan. Cavitation bubble behavior inside a liquid jet. *Physics of fluids*, 19(6):067106, 2007.

[72] Sigurdur T Thoroddsen, K Takehara, TG Etoh, and C-D Ohl. Spray and microjets produced by focusing a laser pulse into a hemispherical drop. *Physics of Fluids*, 21(11):112101, 2009.

[73] Samir Mitragotri. Current status and future prospects of needle-free liquid jet injectors. *Nature Reviews Drug Discovery*, 5(7):543–548, 2006.

[74] J Tanner Nevill, Ryan Cooper, Megan Dueck, David N Breslauer, and Luke P Lee. Integrated microfluidic cell culture and lysis on a chip. *Lab on a Chip*, 7(12):1689–1695, 2007.

[75] Kai Melde, Andrew G Mark, Tian Qiu, and Peer Fischer. Holograms for acoustics. *Nature*, 537(7621):518–522, 2016.

[76] Gary S Settles. *Schlieren and shadowgraph techniques: visualizing phenomena in transparent media*. Springer Science & Business Media, 2012.

[77] JA Mandarino. The gladstone-dale relationship; part i, derivation of new constants. *The Canadian Mineralogist*, 14(4):498–502, 1976.

[78] Zhixin Wang, Alex A Volinsky, and Nathan D Gallant. Crosslinking effect on polydimethylsiloxane elastic modulus measured by custom-built compression instrument. *Journal of Applied Polymer Science*, 131(22), 2014.

[79] WM Lee, A Upadhya, PJ Reece, and Tri Giang Phan. Fabricating low cost and high performance elastomer lenses using hanging droplets. *Biomedical optics express*, 5(5):1626–1635, 2014.

[80] Yu Gao, Chon U Chan, Qiushi Gu, Xudong Lin, Wencong Zhang, David Chen Loong Yeo, Astrid Marlies Alsema, Manish Arora, Mark Seow Khoon Chong, Peng Shi, et al. Controlled nanoparticle release from stable magnetic microbubble oscillations. *NPG Asia Materials*, 8(4):e260, 2016.

[81] Philip J Kitson, Mali H Rosnes, Victor Sans, Vincenza Dragone, and Leroy Cronin. Configurable 3d-printed millifluidic and microfluidic 'lab on a chip'reactionware devices. *Lab on a Chip*, 12(18):3267–3271, 2012.

[82] Chee Meng Benjamin Ho, Sum Huan Ng, King Ho Holden Li, and Yong-Jin Yoon. 3d printed microfluidics for biological applications. *Lab on a Chip*, 15(18):3627–3637, 2015.